

DRAFT VERSION DECEMBER 17, 2024
Typeset using L^AT_EX **preprint** style in AASTeX63

Lessons from the high-resolution spectroscopy of AW UMa and ϵ CrA: Is the Lucy model valid?

SLAVEK M. RUCINSKI¹

¹*Department of Astronomy and Astrophysics, University of Toronto
50 St. George St., Toronto, Ontario, M5S 3H4, Canada*

ABSTRACT

A re-examination of high-resolution spectral monitoring of the W UMa-type binaries AW UMa and ϵ CrA casts doubt on the widely utilized [Lucy \(1968a,b\)](#) model of contact binaries. The detection of the very faint profile of the secondary component in AW UMa leads to a new spectroscopic determination of the mass ratio, $q_{\text{sp}} = 0.092 \pm 0.007$, which is close to the previous, medium-resolution spectroscopic result of [Pribulla & Rucinski \(2008\)](#), $q_{\text{sp}} = 0.101 \pm 0.006$, and remains substantially different from a cluster of generally accepted photometric results by several authors, concentrated around $q_{\text{ph}} = 0.080 \pm 0.005$. A survey of binaries with the best-determined values of the mass ratio shows a common tendency for $q_{\text{ph}} < q_{\text{sp}}$. The tendency for systematically smaller values of q_{ph} may result from the overfilling of the primary lobe and under-filling of the secondary lobe relative to the Roche model geometry, as predicted by the [Stepień \(2009\)](#) model. Despite the observed moderate inter-systemic velocities, the photometric Lucy model may remain useful in providing approximate, though biased, results for the mass ratio. A complicating factor in detailed spectral analysis may be the occurrence of Enhanced Spectral-line Perturbations (ESP) projected over the secondary profiles, appearing in different numbers in the two studied binaries. The ESPs are tentatively identified within the [Stepień](#) model as collision fronts or fountains of primary-component gas from the circumbinary, energy-carrying flow.

Keywords: Eclipsing binary stars (444); W Ursae Majoris variable stars (1783); Spectroscopic binary stars (1557); Close binary stars (254); Astronomical techniques (1684)

1. INTRODUCTION

This paper is a combined re-discussion of the high spectral-resolution time monitoring of two W UMa-type binary stars, AW UMa (Rucinski 2015, paper P1) and ϵ CrA (Rucinski 2020, paper P2). The binaries are located at the high-mass, long-period end of the W UMa-binary effective-temperature sequence. Excellent recent introductions to the current state of research on W UMa-type or contact binaries can be found in Gazeas & Stępień (2008) and Gazeas (2024), while a large collection of data and derived, Lucy-model dependent quantities is in Latković et al. (2021).

The W UMa binaries, sometimes also called “contact binaries”, consist of apparently Main Sequence stars in the spectral range from early F-type to early K-type. W UMa binaries are moderately common in the solar vicinity, with one such system per about 500 F-K dwarfs (Rucinski 2002a). Their kinematic and metallicity properties are characteristic of the old disk population (Rucinski et al. 2013a). The high-luminosity detection advantage of the early F-type systems, such as AW UMa and ϵ CrA, compensates for their smaller numbers compared with somewhat later counterparts and for a tendency to have more dissimilar components, resulting in small variability amplitudes. The mass ratios $q = M_2/M_1$ tend to peak in a wide range around $q \simeq 0.3 - 0.5$ for more common late-F and early-G type binaries, but rarer early-F systems tend to show small values of q and consequently small light variations. There may exist a bifurcation in the mass ratio as a function of the orbital period (Rucinski 2010, Fig.6); this matter is currently a subject of further research (Gazeas 2024).

The similarity of our two targets was not accidental but resulted from a limited availability of telescopes equipped with efficient high-resolution spectrographs that could be used for extended time-monitoring programs. The two objects in question are the brightest W UMa binaries in the sky (with magnitudes $V = 6.8$ and 4.8) making them suitable for observation with a signal-to-noise per spectral-resolution element of around one hundred over a few consecutive nights. Such time-monitoring is resource-expensive, and it is possible that the two objects will remain the only ones observed in this manner for the foreseeable future. This paper brings a comparison and rediscussion of the results from P1 and P2, highlighting that rapid spectral monitoring is one of the few avenues for advancing the currently somewhat stalled research on the validity of the popular Lucy (1968a,b) model for W UMa-type binaries (Webbink 2003), especially considering the new, attractive, yet unstudied model proposed by Stępień (2009); see also Stępień & Kiraga (2013).

In both of the considered here binaries, the early-F type, more massive primary component¹ dominates over its smaller companion in terms of the mass and size. Because of its small mass, approximately ten times smaller in both cases, the secondary is an energetically inert appendage to the primary. It carries the binary angular momentum, produces strong tidal effects and provides a substantial surface area for the combined radiative losses of the system. The two binaries are typical for the W UMa-type binaries in that their secondary components appear as hot as the primaries. This characteristic is unique among binary stars with unequal mass components and is the main defining feature of the W UMa-type binaries.

The small masses and unexpectedly high surface brightnesses of the secondary components in apparently stable W UMa-type systems emphasize the need to determine the mass ratios q with high accuracy. Ideally, these determinations should involve as few initial assumptions as possible. Currently, many determinations of the mass ratios are based on light-curve-synthesis photometric

¹ It is proposed to avoid the photometric definition of the “primary component” in favor of the more physical one based on the mass.

solutions which utilize the relatively complex Lucy (1968a,b) model, where q_{ph} is one of its many parameters. In contrast, spectroscopic determinations, through a ratio of orbital semi-amplitudes, $q_{\text{sp}} = K_1/K_2$, are expected to reflect global binary dynamics directly but are observationally more challenging to determine.

This paper focuses particularly on the observational properties of the secondary components and the energy-transport mechanisms that lead to their high surface brightnesses. We also address the good agreement between the photometric and spectroscopic determinations for ϵ CrA at $q = 0.13$ (Section 3) and the continuing substantial discrepancy for AW UMa (Section 4). For AW UMa, the medium-resolution result of Pribulla & Rucinski (2008), $q_{\text{sp}} = 0.101 \pm 0.006$, significantly differs from the widely accepted $q_{\text{ph}} \simeq 0.08$, based on several photometric studies starting from Mochnacki & Doughty (1972a) and ending with Wilson (2008).

We note that before P1, there have been several previous short-duration attempts to observe AW UMa spectroscopically (Paczyński 1964; McLean 1981; Anderson et al. 1983; Rensing et al. 1985; Rucinski 1992). These efforts mainly focused on *detecting* the spectroscopically faint secondary component and confirming the photometric mass ratio. The DDO analysis of Pribulla & Rucinski (2008) was the first to provide a larger amount of data. In contrast, ϵ CrA was analyzed spectroscopically using a cross-correlation function (CCF) approach only once by Goecking & Duerbeck (1993), followed by the high-quality high-resolution spectral analysis reported in P2. The previous line-by-line measurements for the primary component of ϵ CrA by Tapia & Whelan (1975) currently have a very limited value.

A general description and comparison of both binaries in terms of their general properties is in Section 2. Sections 3 and 4 discuss the complex appearance of the secondary components as seen in spectroscopy. In these sections, the new term Enhanced Spectral-line Perturbation (ESP) is introduced to describe radial-velocity-defined features of increased density of the primary-component gas, projected onto the secondary component profile. A newly detected, very faint signature of the secondary component in AW UMa confirms the “large” value of q_{sp} of about 0.10.

Section 5 demonstrates that the tendency for $q_{\text{ph}} < q_{\text{sp}}$ is a common feature in the best mass-ratio determinations of other W UMa binaries. The previously unrecognized weaknesses of the Lucy model in providing unbiased values of q_{ph} are discussed in Section 6. As discussed in Section 7, the tendency for $q_{\text{ph}} < q_{\text{sp}}$ cannot be explained by the Lucy model but is consistent with the Stępień (2009) model. Section 8 discusses the implications of the presented results and suggests possible directions for future research.

2. THE TWO BINARIES AS SEEN IN RADIAL VELOCITIES

All results presented in papers P1 and P2 were based on the radial velocity (RV) profiles obtained through the analysis of individual spectra using the linear, Broadening-Functions (BF) deconvolution technique (Rucinski 2002b, 2010, 2012). The technique is computationally more demanding than the inherently non-linear, easier-to-implement Cross-Correlation Function (CCF) technique; it provides high-quality RV profiles in reference to the shape and strength of the spectral lines for a star of the same spectral type. The CCF technique is simpler but adequate for measurements of well-peaked mean profiles; line-by-line RV measurements are practically impossible for W UMa-type binaries due to extreme broadening and blending of the spectral lines. The BF profiles should not be interpreted as RV-projected images of a binary system; to do so, an assumption of a solid-body rotation is

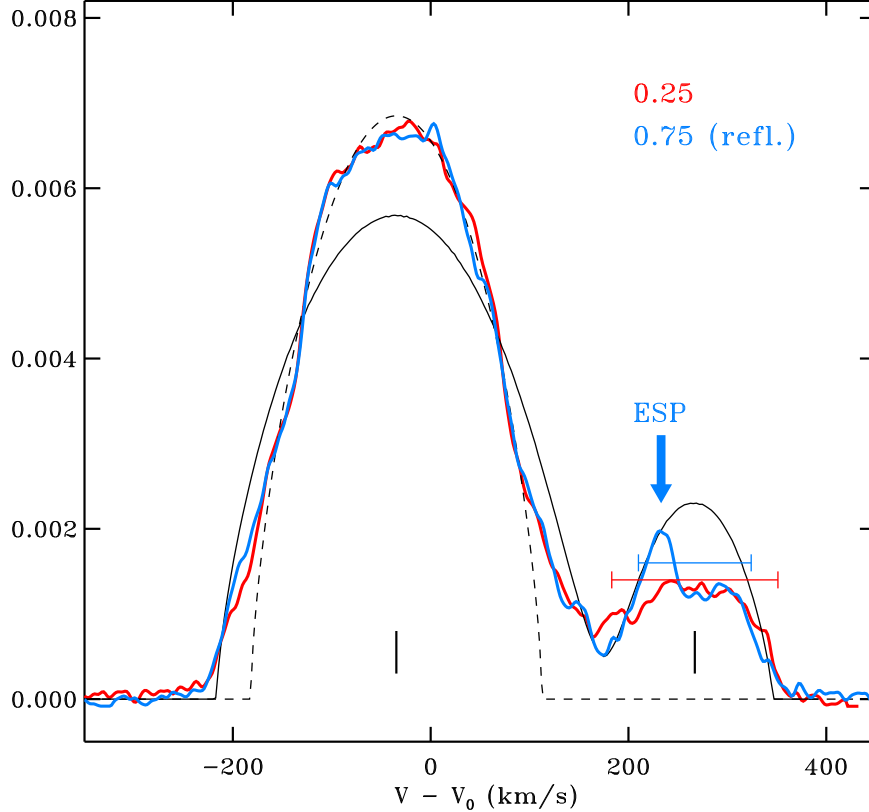


Figure 1. The BF profiles for ϵ CrA at both orbital quadratures, i.e. phases $\phi = 0.25$ (red) and $\phi = 0.75$ (blue), in units per a RV sampling interval of 8.5 km s^{-1} . The profile $\phi = 0.75$ is inverted in the velocity scale with the common origin at the RV of the binary mass center at $V_0 = -62.54 \text{ km s}^{-1}$. The Lucy-model profile for the orbital phase $\phi = 0.25$ and the assumed mass ratio $q = 0.13$, the fill-out parameter $f = 0.25$ is shown by a thin black line. Vertical dashes mark the mass-center RV's while a thin, broken line shows the rotational profile fit to the primary component. The red and blue bars over the secondary component show the widths of the secondary profile observed at both orbital quadratures. An Enhanced Spectral-line Perturbation (ESP) affecting the secondary profile at $\phi = 0.75$ is pointed by an arrow at 235 km s^{-1} .

necessary; generally, we do not know the spatial location of a given RV feature. Strict solid-body rotation is a basic assumption of the Lucy model, yet determining the correct model is precisely the main subject of our investigation.

As with other spectral deconvolution process, the BF technique has the limitation of being sensitive to the presence of dispersed matter in the binary system: Any *emission* component in observed line spectra would produce a dip or would weaken the restored velocity profile, while any *absorption* would produce stronger features in BF profiles. In general, deviations from a standard, stellar-atmosphere optical-depth dependence of the source function can modify the profile. The BF technique, thanks to its linear properties, tends to show such deviations more directly than the CCF technique.

The data for AW UMa (P1) and ϵ CrA (P2) were analyzed with the spectra resampled to the same spectral resolution of 8.5 km s^{-1} (the resolving power $R \simeq 35,000$), with the final RV profiles for ϵ CrA being of much better quality: The median signal-to-noise ratio per resolution element of $S/N = 57$ was for AW UMa (P1) and $S/N = 120$ for ϵ CrA (P2). We show two typical RV profiles for ϵ CrA at both orbital quadratures in Figure 1. Typical profiles for AW UMa are very similar, but are much

more complex and variable within the secondary component parts and exhibit larger observational noise.

Here is a summary of similarities and differences between the two binaries:

1. In both binaries, the upper two-thirds of the primary component profile is narrower than predicted by the Lucy contact-binary model but agrees very well with a standard profile for a single star of a smaller radius rotating at the orbit-synchronous rotation rate (sizes 88% and 85% of the critical Roche-lobe side radius for AW UMa and ϵ CrA, respectively). This property was recognized in AW UMa already by [Rensing et al. \(1985\)](#) using photographic spectra. The base of the primary profile in both binaries, referred to as the “pedestal” in P1, is roughly as wide, as predicted by the Lucy model. The narrow primary profile may be due to the anticyclonic circulation around the rotation pole of the mass-losing primary, as predicted by the hydrodynamic model of [Oka et al. \(2002\)](#), while the wide pedestal is explained by the binary circulation model of [Stępień \(2009\)](#). These observational properties contribute to our discussion of an appropriate model for W UMa binaries in Section 7.
2. In both binaries, the primary-component profile widths show a small tidal distortion (line-of-centers elongation) of the more massive star of $< 5 \text{ km s}^{-1}$. This number should be compared with the mean values of $V \sin i \simeq 181 \text{ km s}^{-1}$ for AW UMa (P1, Fig. 3) and $V \sin i \simeq 147 \text{ km s}^{-1}$ for ϵ CrA (P2, Fig. 3). These width variations are partly masked by greater noise in AW UMa but are better defined for ϵ CrA.
3. The primary component of AW UMa showed a network of “ripples” or non-radial pulsations partly extending into the profile pedestal. The ripples, which are visible after subtraction of the stable mean profile (Figures 8, 9, 10 in P1), look very similar to the non-radial pulsations detected (subsequently to the work reported in P1) in the rapidly rotating, bright star Altair (α Aql, A7V, $V \sin i \simeq 240 \text{ km s}^{-1}$ ([Rieutord et al. 2023, 2024](#))) which is a δ Sct-type star. So far, there has been no attempt to detect photometrically these small, rapid pulsations in AW UMa. The primary of ϵ CrA appears to be entirely free of non-radial pulsations; they would be easily detectable because of the higher S/N of its spectra.
4. The secondary-component RV profiles of both binaries show significant deviations from the predictions of the Lucy model. They appear much weaker and flatter, which may indicate either a genuine faintness of the secondaries or a different (later) spectrum that does not match the template used in the BF determination.
5. The secondary-component profiles in both binaries were distorted by narrow perturbations of increased intensity of absorption lines. The disturbances, referred to as “wisps” in P1 and P2 due to their visibility in time sequences of the RV profiles, systematically shifted with the orbital phase, complicating our interpretation of the secondary component profile in AW UMa. See Figure 13 in P1 for an illustration of their confusing appearance. The wisps do not appear to result from the Struve-Sahade effect ([Gies et al. 1997](#); [Linder et al. 2007](#)), which is observed in early-type stars. The S-S effect describes the increased strength of spectral lines of the approaching star over half of the orbital period. In contrast, the wisps in AW UMa and ϵ CrA are narrow, well-localized in radial velocities, and their phase migration allows their approximate geometric localization within the binary structure (Sections 3 & 4).

6. ϵ CrA (P2) showed one well defined, strong, narrow “wisp”. However, an identical, strong feature appeared also in AW UMa – albeit among typically three to four wisps present there at a time. The phase evolution of this prominent wisp can be interpreted as due to a localized region of the primary-component gas overlying the secondary component profile. Its location in both stars was estimated at the sub-observer orbital phase $\phi = 0.65$ and may correspond to a collision front of the gas striking the primary after circulating the secondary component. The disturbance was very stable and remained visible in ϵ CrA during the whole observing run of the 28 orbital revolutions of the binary. It is marked by an arrow in the $\phi = 0.75$ profile in Figure 1; its orbital-phase evolution is discussed in Section 3. In this paper, we introduce the term Enhanced Spectral-line Perturbations (ESP) to stress that such perturbations in Broadening Function profiles correspond to stronger absorption spectra due to spacially-localized gas atoms having the same atomic excitation properties as those of the early-F type primary star.
7. The better data quality and somewhat simpler profiles permitted the detection of weakly defined outermost edges of the secondary-component velocity profile in ϵ CrA (P2). Since both edges were detected, the velocity field on the secondary seemed to be well confined, similar to that of a detached star. The mean velocity from the edges – assumed to be that of the secondary mass center – showed an approximately sine-curve phase dependence, as expected in anti-phase to that observed for the primary component. The semi-amplitude K_2 derived in this way led to a mass ratio $q_{\text{sp}} = K_1/K_2 = 0.130 \pm 0.001$, in general consistency with the photometric Lucy-model estimates, $q_{\text{ph}} = 0.114 \pm 0.003$ (Twigg 1979) and 0.1244 ± 0.0014 (Wilson & Raichur 2011). Unfortunately, a similar direct determination of K_2 for AW UMa in P1 could not be done due to the simultaneous presence of several ESPs affecting the secondary-component profile. Indirect estimates in P1, based on the poorly-defined mean profile shape suggested a value of the mass ratio $q_{\text{sp}} \simeq 0.10$.
8. The edge-to-edge widths of the ϵ CrA secondary-component RV profile appeared to differ for the two orbital quadratures. Expressed as the observed half-widths, they were approximately 90 km s^{-1} at $\phi = 0.25$ and 70 km s^{-1} at $\phi = 0.75$. This unexplained variability is marked by horizontal bars over the secondary-component profiles in Figure 1. This subject is discussed further in Section 3.
9. No parallel photometry was conducted during the spectroscopic programs described in P1 and P2. Information restored from the available spectra (Figure 2 in P1; Figure 13 in P2) reveals different and complex phase variations of the integrated strength of all spectral lines in the used BF window for the two binaries.
10. The spectroscopic data do not provide information on the orbital inclinations of either binary. A difference in the photometric variability amplitudes suggests that the ϵ CrA orbit is viewed at a slightly more inclined angle than AW UMa. The tentative assumptions of the previous, Lucy-model photometric estimates (Sec. 1) are $i \simeq 78^\circ - 80^\circ$ for AW UMa and $i \simeq 72^\circ - 73^\circ$ for ϵ CrA, though these are not explicitly used in the paper. It may be useful to note that for ϵ CrA, we can possibly observe the volume between the components during the transit eclipse ($\phi = 0$), with a line-of-sight passing “above” the secondary component (see Figure 3).

11. Although they have the same spectral type and a similar, small mass ratio, the binaries are definitely *not identical*: Their orbital periods differ substantially: 0.4387 days for AW UMa and 0.5914 days for ϵ CrA. The observed maximum-light V magnitudes are 6.84 and 4.74, and the parallax data, 14.78 mas and 31.81 mas for AW UMa and ϵ CrA respectively (Gaia Collaboration 2020). These values give the absolute maximum-light magnitudes $M_V = 2.69$ for AW UMa and 2.25 for ϵ CrA. The longer period and the higher luminosity of ϵ CrA align with its larger primary mass, as discussed in P1 and P2.
12. Both binaries appear to systematically change their orbital periods, showing well-defined parabolic variations in the $O - C$ eclipse moments, but *in the opposite sense*: In AW UMa the period shortens (Rucinski et al. 2013b), while in ϵ CrA the period lengthens (P2). The respective timescales are $(-2.3 \pm 0.1) \times 10^6$ yrs and $(+1.26 \pm 0.04) \times 10^6$ yrs. AW UMa has a physical, G7V proper-motion companion $67''$ away ($> 4,600$ AU), while no third body has been detected for ϵ CrA so far.

3. THE SECONDARY COMPONENT OF ϵ CRA

The secondary components keep the secret of the moderate mass transfer and large energy transfer between the component stars in W UMa-type systems such as ϵ CrA and AW UMa. These processes are critical to understanding the relatively long duration of the contact phase in these systems. The following sections will describe the observed properties of the secondary components, beginning with ϵ CrA and then moving on to AW UMa. This sequence deviates from the analysis order in the previous studies (P1 and P2), prioritizing the simpler and more thoroughly observed ϵ CrA to more effectively elucidate the shared features. For ϵ CrA, we rely on the previously established orbital semi-amplitudes, K_1 and K_2 , as reported in P2, without any modifications. The focus will be on the lessons learned from the case of ϵ CrA and how they could be applied to understanding AW UMa, as discussed in Section 4.

As described in P2, the secondary component was relatively easy to detect in the radial velocity profiles of ϵ CrA. While no distinct peak or profile centroid could be detected, the range or extent of the profile was well defined by “edges” on images derived from the RV profiles. The presence of such RV edges made the secondary component profiles dramatically different from that predicted by the Lucy model and resembling those for a velocity field on a detached binary component.

The profiles were significantly fainter and flatter than those expected by the Lucy model (Figure 1). However, the extremes of the observed profiles were consistently well-defined to assume that their mean values could correspond to the motion of the secondary mass center. These values varied in anti-phase to the orbital motion of the primary component, allowing the derivation of the semi-amplitude K_2 . This finding stands in stark contrast to the complex appearance of the secondary-component profiles in AW UMa (P1, Figure 13). However, the differences in data quality and quantity between the studies of ϵ CrA and AW UMa could influence this comparison, potentially favoring ϵ CrA due to its better data quality and phase coverage.

The two main complications in the secondary-component profiles of ϵ CrA were: (1) The half-extends or half-widths of the profile (functionally similar to $V \sin i$ in rotating stars) showed variations with phase, and (2) a moving, phase-dependent, “spiky” feature, what we call “Enhanced Spectral-line Perturbation” (ESP) was observed in the orbital phases $0.5 < \phi < 1.0$ (see Figure 1). The first

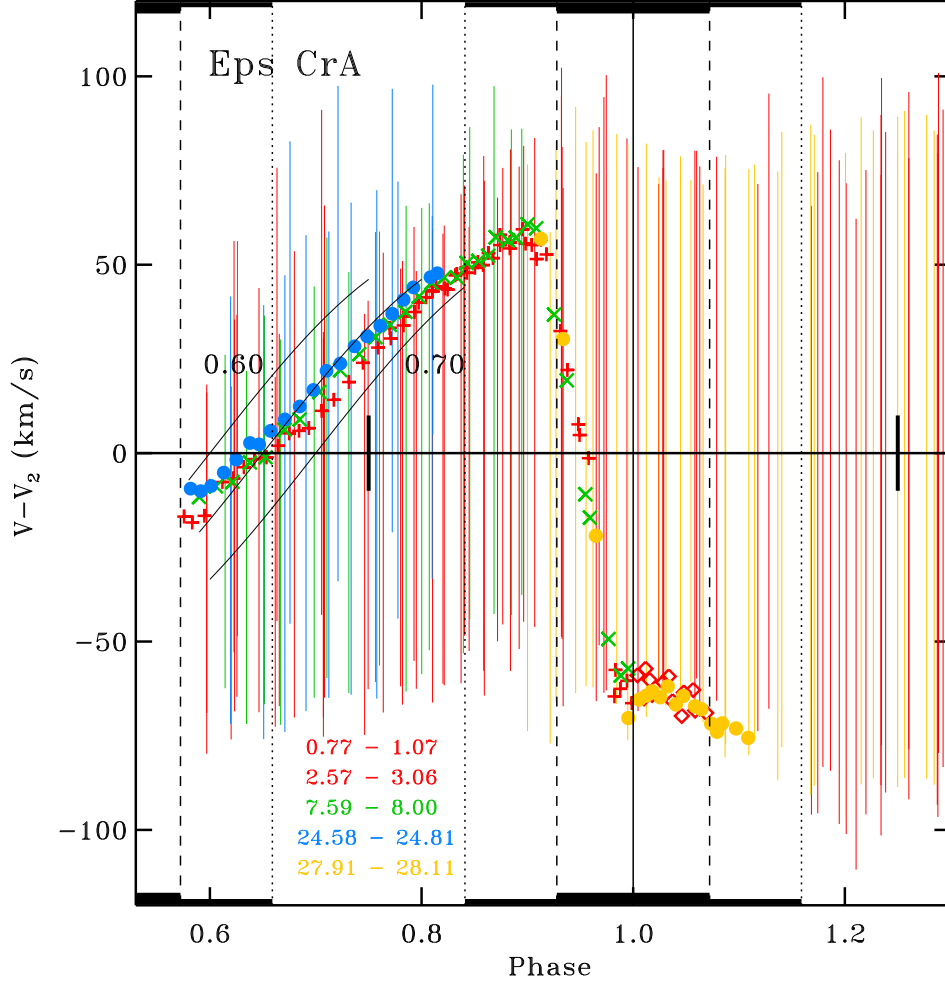


Figure 2. The thin vertical bars show measurements of the edge-to-edge extent of the secondary component RV profiles for ϵ CrA, expressed relative to the velocity of the secondary component’s mass center. These repeated and difficult estimates were derived from images formed from individual Broadening Function profiles. The broken wavy lines give the expected range of velocities for the inner critical Roche lobe of the mass ratio $q = 0.130$. Observations from individual nights are color-coded as per the legend in the figure, where the integer part of the phase gives the number of elapsed orbits from the assumed initial epoch (see P2). Thick black lines at the upper and lower figure frames indicate the phase ranges of the estimated total and partial eclipses. In the left part of the figure, the phase drift of the dominant Enhanced Spectral-line Perturbation (ESP) is represented by colored symbols according to the figure legend. The inclined lines alongside these symbols represent the predicted phase drifts for three sub-observer longitudes, expressed in orbital phases: 0.6, 0.65, and 0.7.

complication was noted only briefly in P2. It is shown in Figure 2 as the full measured extent of the secondary component profile, relative to the assumed sine-curve motion of the secondary with $K_2 = 267 \text{ km s}^{-1}$. The widths were determined from images similar to Figures 5 – 9 in P2, rather than from individual RV profiles; this provided a better definition of the measurements. The phase range in Figure 2 is limited to the phases when the secondary component is expected to be in front of the primary, $0.58 < \phi < 1.42$. Trends in the secondary-component RV widths in Figure 2 appear to be well established: The profile is noticeably narrower ($\simeq 70 \text{ km s}^{-1}$) around $\phi \simeq 0.75$ and wider ($\simeq 90 \text{ km s}^{-1}$) around $\phi \simeq 0.25$ where the velocity range is similar to that for a solid-body rotation

of the critical Roche-model lobe. The deviations from a sine-curve, while relatively small ($20 - 30 \text{ km s}^{-1}$) compared with the large value of K_2 , are definitely systematic. Their presence does not affect the essential anti-symmetric phase variation relative to the primary, yet it is concerning. We do not have a simple explanation for them beyond expectations that the velocity field over the secondary component may be complex and that the outer layers of the secondary are seen at constantly changing orientation and thus oblique-view, optical-depth accumulation.

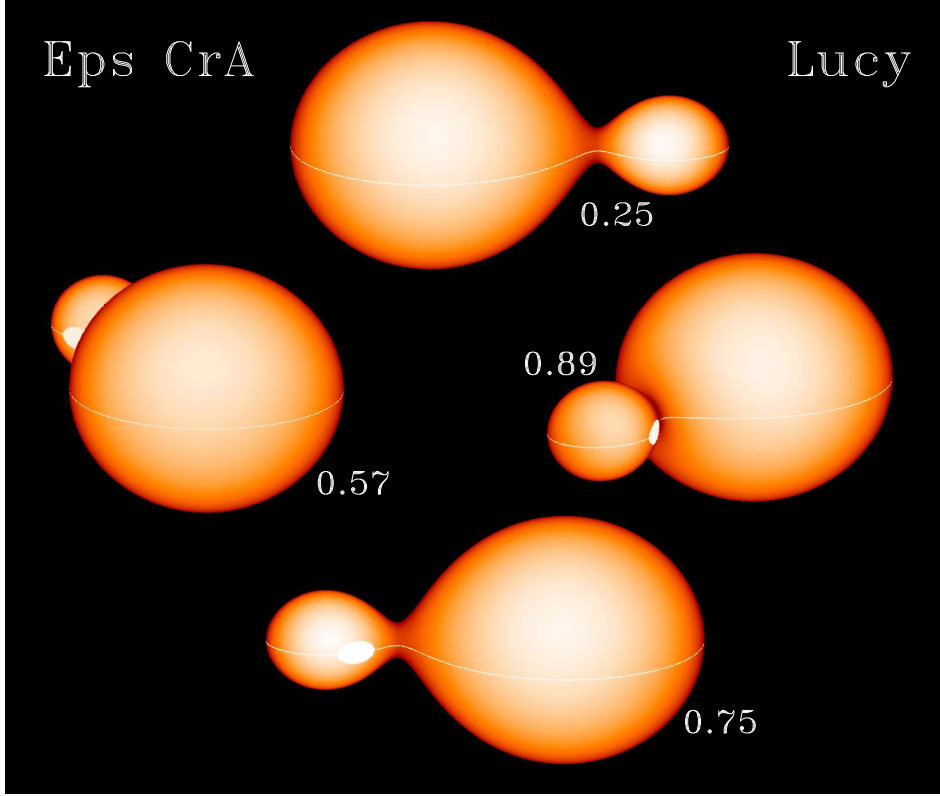


Figure 3. A schematic view of ϵ CrA at four orbital phases, as indicated in the figure. The Lucy model with the mass ratio $q = 0.13$, the fill-out parameter $f = 0.25$ and the orbital inclination $i = 73$ degrees were assumed in generating these images. The orbital phases $\phi \simeq 0.57$ and $\phi \simeq 0.89$ correspond to the orientations when the region of the Enhanced Spectral-line Perturbation (ESP), shown as a white patch, comes into view or is about to disappear behind the edge of the secondary component. Except for the approximate location in longitude, the geometry and extent of the ESP-causing region in the stellar latitude are unknown and arbitrary in the figure (see the text).

The second complication of the ϵ CrA secondary-component profile, the prominent ESP visible in the phase range $0.57 < \phi < 0.89$ (Figure 2) requires special attention due to its location, strength and persistence. During each observed binary orbit, the region emerged at $\phi \simeq 0.57$ with the RV around -10 km s^{-1} relative to the secondary center, then drifted to positive velocities reaching about $+55 \text{ km s}^{-1}$ at $\phi \simeq 0.89$ where it started overlapping with the primary component profile. Constraints on the ESP location within the binary can be derived utilizing the orbital-phase dependence of the RV variations. The simplest model would be a region anchored to the secondary component, with the observed phase variations caused by the variable component of the observer-directed product $\vec{r}\Omega$. Here, \vec{r} gives the spatial position of the active ESP region relative to the secondary center and Ω is

the angular rotational velocity of the binary. The inclined lines in Figure 2 give predictions of such a phase dependence for an ESP located on the equator of the secondary component of the inner critical Roche equipotential at three sub-observer points, $\phi = 0.60, 0.65, 0.70$. The zero RV crossing by the drift line suggests a position on the secondary component at the sub-observer position $\phi \simeq 0.65$. Lucy-model generated images of ϵ CrA with the ESP located at that longitude are shown for four orbital phases in Figure 3.

To be detected as a positive intensity deviation in the BF, the gas producing the feature must possess properties similar to those of the outer layers of the primary component, with the same atomic-excitation properties. This is a direct result of the BF determination process which used a high-temperature, early-F type spectrum as a reference. The ESP is visible on the hemisphere centered at $\phi = 0.75$, which is on the opposite side to where a Coriolis-force-deflected flow from the primary would be expected. Therefore, the stream of matter must have circled the secondary component to collide with some obstacle, forming a fountain or a collision front. We return to this subject in the discussion of the contact binary model in Section 7.

The ESP strength did not seem to vary with the orbital phase within the observed interval $0.57 < \phi < 0.89$ and remained at an intensity of about 1.5% to 2% ($\pm 0.2\%$) relative to the mean integrated Broadening Function². It was also surprisingly stable over the entire duration of our ϵ CrA campaign, remaining at the same place on five observing nights within 28 binary orbits, i.e. for over 2 weeks. Although the active region was placed on the equipotential surface in Figure 3, its spatial location is not well defined; it may be in the space overlying the secondary, possibly as in Figure 9 in the discussion of the Stępień model in Section 7.2.

A detailed analysis of the images formed from the BF profiles for ϵ CrA indicated an additional feature in the secondary-component profile that was not discussed in P2: The hot gas that produced the ESP remained at least partially visible during the transit-eclipse phases. As shown in Figure 4, after encountering the primary profile at $\phi \simeq 0.89 - 0.90$, the ESP stopped shifting in heliocentric radial velocities and stabilized at about -75 km s^{-1} relative to the binary mass center. This orientation corresponded to the rapid variation of its RV relative to the secondary mass center. All of this happens in projection over the large primary-component disk (Figure 2). Because of the relatively low orbital inclination of ϵ CrA of $i \simeq 72^\circ - 73^\circ$, it is possible that – thanks to the line of sight passing *above* the secondary – we see here the volume between the binary components. This orientation can be visualized for transit-eclipse phases $\phi > 0.90$ in Figure 3. From about $\phi \simeq 0.98$ onward, just before the mid-eclipse, the active region became visible at negative velocities (Figure 4), presumably on the observer-approaching side of the secondary component. This may be produced by the fresh, hot gas from the primary sliding along the surface of the secondary component.

4. THE SECONDARY COMPONENT OF AW UMA

The most extensive previous spectroscopic investigation of the AW UMa orbit by Pribulla & Rucinski (2008) was conducted at a medium spectral resolution with data collected at the David Dunlap Observatory (DDO) over ten non-consecutive nights. The mean secondary component profile was used to derive the semi-amplitude K_2 and then the mass ratio, $q_{\text{sp}} = 0.101 \pm 0.006$. This

² The BF integral was close to unity through the selection of the stellar template of a spectral type similar to that of the primary component; see P2 and the lower panel of Fig. 13 there.

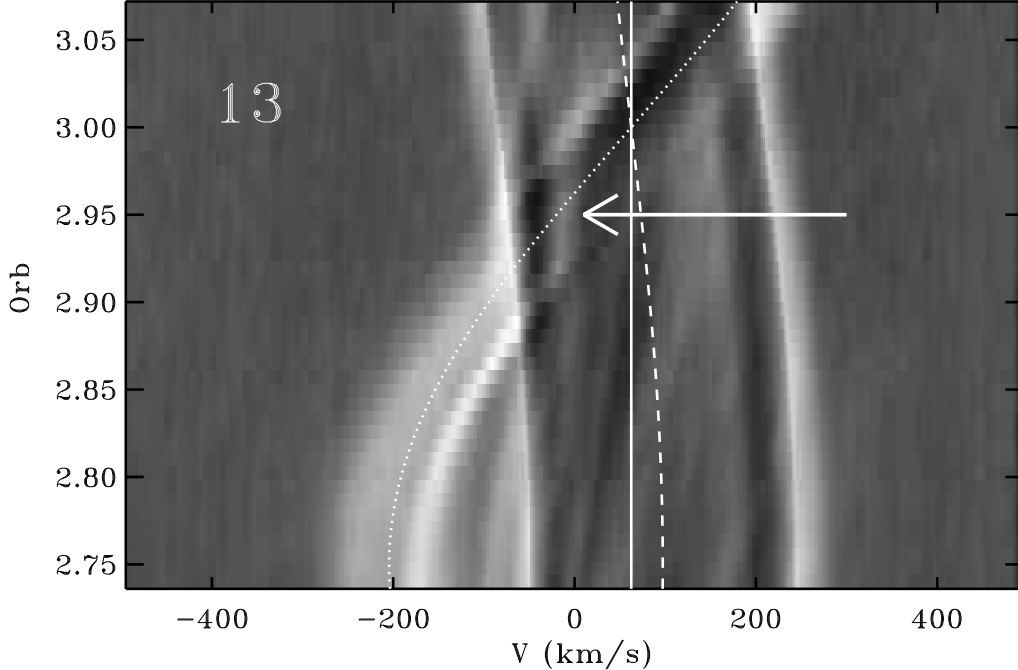


Figure 4. The orbital-phase evolution of the Enhanced Spectral-line Perturbation (ESP) on the secondary component of ϵ CrA during the transit eclipse. The horizontal axis shows the radial velocity in the heliocentric system while the vertical axis gives the time (increasing upwards) expressed in orbital periods, *Orb*; the eclipse centre on the observing night #13 was located at $Orb = 3.0$ (see P2). The ESP localized at the sub-observer point at $\phi \simeq 0.65$ (as described in the text and in Figure 2), possibly continued its evolution into the eclipse phases and merged with other spectral-line intensity features. The mass-center velocities of both stars are shown by broken (primary) and dotted (secondary) sine-curve lines.

value was larger than any of the previous Lucy model photometric determinations, which tended to concentrate around $q_{\text{ph}} \simeq 0.08$.

With only three available nights and given a highly complex secondary-component profile, the P1 analysis could provide only a tentative confirmation of the $q_{\text{sp}} \simeq 0.10$ result. We re-discuss the results of P1 in light of the experience gained in analyzing the simpler and better-observed ϵ CrA binary (Section 3). It should be taken into account that only five orbital revolutions over three nights – with interruptions – were available for AW UMa. As for ϵ CrA, a search was made for (1) distinct RV edges of the secondary component profile (as for a detached star) that (2) would move in anti-phase to the motion of the primary component of the binary. They have been detected, but they are less distinct than in ϵ CrA due to the presence of several variable ESPs (see Figures 8 – 10 of P1). An example of the edges is shown in Figure 5 where they are marked by arrows. The heliocentric velocities of the edges are listed in Table 1.

With the new RV data for the secondary component, we attempted a determination of the spectroscopic orbital elements for AW UMa. Of the available 584 radial velocities for the primary component and 118 measurements for the secondary, the orbital solution used 340 velocities within $0.2 < \phi < 0.8$ as listed in Table 3 of P1 and all 118 measurements of the profile edges E_1 and E_2 , as listed in Table 1. The mean values from the edges were used to represent the motion of the secondary component.

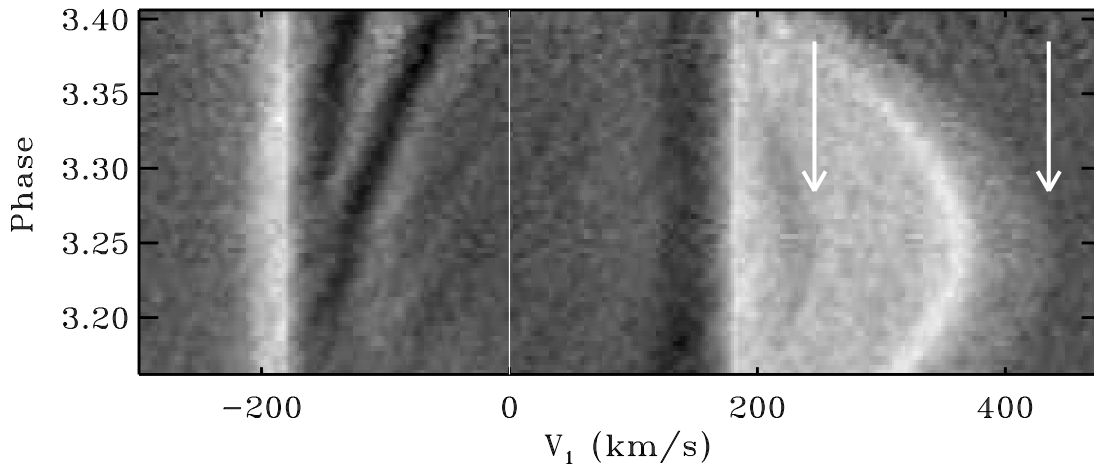


Figure 5. A segment of the 2D image formed from individual BF’s arranged in orbital phase for the second of the available three observing nights of AW UMa; it is a part of Figure 9 in P1. The radial velocities (the horizontal axis) are in the system centered on the primary component with the strong rotational profile of the primary component subtracted from the BF profiles for better visibility of the secondary component. The orbital phases (the vertical axis), are expressed as a full count of orbital cycles from the assumed initial epoch, as in P1. The edges of the secondary component profile, as marked by the arrows, E_1 and E_2 , were determined from images similar to this one. Note that the strongly non-uniform distribution of intensity across the secondary-component profile and the presence of the bright RV “wisp” which is identified in Figure 7 as ESP #4.

Table 1. AW UMa: Radial velocities of the secondary-component profile edges

Phase (<i>Orb</i>)	E_1 (km s $^{-1}$)	E_2 (km s $^{-1}$)
0.604	−303.33	−178.28
0.632	−336.09	−206.07
0.636	−334.82	−213.09
0.674	−379.83	−237.40
0.681	−377.60	−243.44

NOTE— The first column gives the time expressed in orbital phase counted continuously from the assumed initial epoch (the *Orb* units, as defined in P1).

The second and third column give the heliocentric radial velocities of the edges of the secondary component profile, E_1 and E_2 expressed in km s $^{-1}$, as explained in the text. This table is available in the on-line version only.

The orbital solutions for AW UMa are given in Table 2. The first two lines quote the results for the primary component from P1, while the last line gives the combined final solution for the three parameters V_0 , K_1 and K_2 . The solution is well-defined thanks to the simultaneous constraint on

Table 2. AW UMa: Orbital solutions

#	V_0 km s ⁻¹	K_1 km s ⁻¹	K_2 km s ⁻¹	Comment
1	-15.90 ± 0.12	28.37 ± 0.37		From P1, $0.25 < \phi < 0.75$, 299 obs.
2	-15.88 ± 0.06	29.08 ± 0.09		same for $0.20 < \phi < 0.80$, 340 obs.
3	-14.57 ± 1.13		314.06 ± 1.18	$0.15 < \phi < 0.35$ and $0.65 < \phi < 0.85$, 45 obs.
4	-15.74 ± 0.14	29.08 ± 0.09	314.32 ± 1.17	Combined solution, phases as for #2 and #3.

NOTE— The solution uncertainties were estimated as standard ($\pm 1\sigma$) errors by a bootstrap-sampling experiment based on 10,000 repetitions. The bootstrap parameter distributions did not show any obvious asymmetries.

Table 3. The orbital parameters of AW UMa

Parameter	Result	$\pm\sigma$	Unit
P	0.4387242		day
$HJD(pri)$	2455631.6498		day
V_0	-15.74	0.14	km s ⁻¹
K_1	29.08	0.09	km s ⁻¹
K_2	314.32	1.17	km s ⁻¹
$q_{sp} = M_2/M_1$	0.092	0.007	
$A \sin i$	2.977	0.001	R_\odot
$(M_1 + M_2) \sin^3 i$	1.841	0.019	M_\odot
$M_1 \sin^3 i$	1.685	0.020	M_\odot
$M_2 \sin^3 i$	0.156	0.0026	M_\odot

NOTE— The errors are the formal least-squares errors and do not reflect possible systematic uncertainties in the data.

V_0 from the motion of both components and the RV's of the secondary component following the sine curve. The uncertainties of the RV parameters V_0 , K_1 and K_2 in Table 2 were determined by bootstrap-sampling experiment. While the formal random errors estimated this way appear to be small, systematic errors may be larger because of the lack of a proper velocity-field description on the stellar disks.

The radial velocity variations for both components are shown in Figure 6. It is similar to Figure 4 in P1, but with the secondary-component orbit added using the velocity scale reduced by 10 times relative to that for the primary component. Table 3 gives the derived parameters of the binary. Please note that the value of K_2 in Sec. 7.1 of P1 was incorrectly given to the sum of the semi-amplitudes; the correct numbers are given here.

The new radial-velocity solution, as shown in Figure 6, confirms the previously noticed negative deviations of the primary-component radial velocities after the transit mid-eclipse, in the wide phase range $0 < \phi < 0.25$. Contrary to what was suggested in P1, the RV deviations do not appear

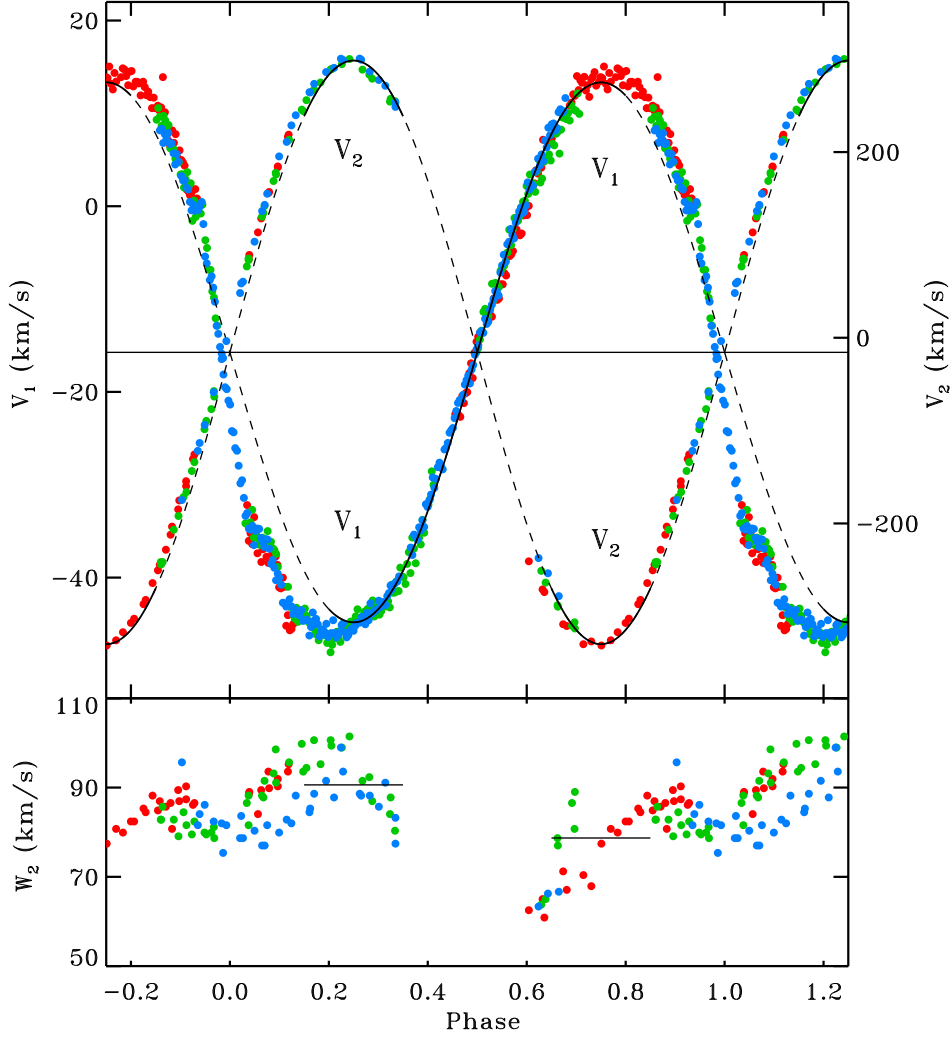


Figure 6. The heliocentric orbital velocities of both AW UMa components. The figure corresponds to Figure 4 in P1, with added velocities of the secondary component, derived as the mean values of the secondary profile edges E_1 and E_2 . The scale for the secondary (the right vertical axis) is compressed 10 times relative to that for the primary and is shifted to the same V_0 . The three observational nights of AW UMa are coded by color: 1 – red, 2 – green, 3 – blue. The continuous lines show the sine curve fits to the data; the dashed line parts correspond to the phase intervals which were not used in the fits because of mutual interference of the wide component profiles. The lower panel shows the half-width of the secondary component profile, $W_2 = (E_2 - E_1)/2$, which for a standard rotational profile would correspond to the apparent equatorial velocity $V_2 \sin i$.

to result from the “Rositter – McLaughlin” effect since we see only *a trace of positive deviations before* the mid-eclipse. Thus, the deviations are asymmetric relative to the line joining the mass centers. The change is forced mostly by the shift in V_0 , caused by the inclusion of the secondary orbit. The phases immediately after the mid-eclipse correspond to the orientation of the binary with the Coriolis-deflected flow from the primary directed at the observer.

The negative RV deviations reach about -10 km s^{-1} and, surprisingly, the whole, broad profile has acquired such a negative shift as if the whole hemisphere of the primary were approaching the observer. There exists a corresponding negative deviation after the mid-eclipse in $\epsilon \text{ CrA}$ (see P2,

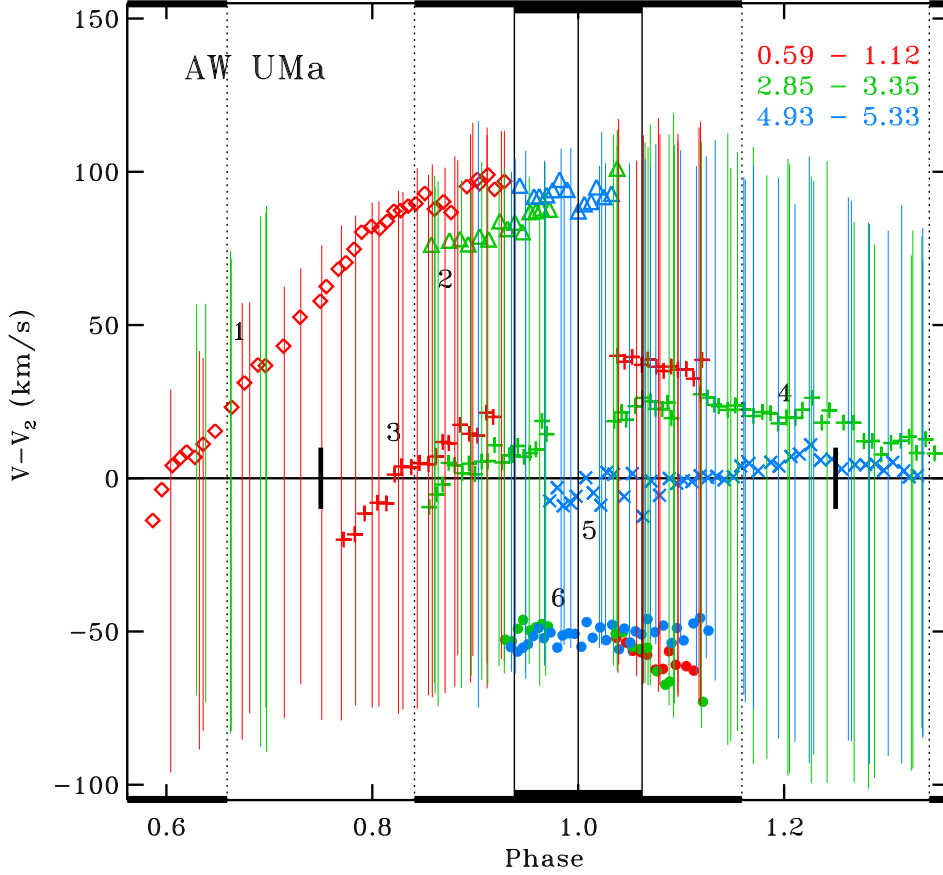


Figure 7. The figure shows the AW UMa secondary-component measured velocity extent as vertical lines coded in color by the phase range of the observing night; see the legend in the right upper corner of the figure. The figure is similar to the one for ϵ CrA (Figure 2) where other details are explained. The numbered Enhanced Spectral-line Perturbations (ESPs) observed on individual nights are discussed in the text.

Fig.4), but it is smaller, on the order of -3 km s^{-1} and much more localized in the phase range. The current restriction of the AW UMa primary data to the phase range $0.20 < \phi < 0.80$ is an attempt to eliminate those (poorly understood) profile distortions and thus restore symmetry relative to the line joining the two mass centers.

We note that the primary profiles were observed to briefly broaden during the primary eclipse phases in both binaries (see Fig. 3 in P1 and Fig. 3 in P2), but the width variations seemed to be symmetric relative to the primary eclipse mid-eclipse phase. The findings of the mean velocity shift and the broadening symmetry may be important in understanding the mass outflow from the primary component.

The radial velocities of the secondary component of AW UMa, as derived from the two profile edges E_1 and E_2 , generally follow the anti-phase variations relative to the primary motion, but with the similar irregularities to those observed in ϵ CrA:

1. The half-widths, $W_2 = (E_2 - E_1)/2$, are systematically variable: At the first quadrature $W_2(0.25) = 91 \pm 3 \text{ km s}^{-1}$ while at the second quadrature $W_2(0.75) = 79 \pm 3 \text{ km s}^{-1}$ (the lower panel of Figure 6);

2. The mean velocities show $\pm 30 \text{ km s}^{-1}$ deviations from the expected sine shape (Figure 7); they can be considered moderate relative to the large semi-amplitude $K_2 = 314 \text{ km s}^{-1}$, but are systematic.

These irregularities, similar to those observed in $\epsilon \text{ CrA}$ (Section 3, Figure 2) probably reflect changes in the spectral-line optical depth for the rapidly changing geometry of the binary system.

While the extent and motion of the underlying secondary-component profiles in AW UMa and $\epsilon \text{ CrA}$ appear to be similar, the two binaries differ in the type and number of the ESPs. One strong ESP was visible for $\epsilon \text{ CrA}$ on all nights (Figure 2); it always showed the same phase drift as the binary rotated. In contrast, in AW UMa two to four ESPs were simultaneously visible (Figure 7) at different locations within the secondary component profile. One of these was very similar to that in $\epsilon \text{ CrA}$, while the others appeared more irregular showing migration within hours and sometimes reappearing after the observing daytime breaks. The ESPs were typically stronger than the underlying profile; an example, ESP#4, is visible in Figure 5.

The very short period of AW UMa created another complication in attempts to follow the evolution of individual ESPs: expressed in the binary orbital cycles, the CFHT observations experienced relatively long daily breaks amounting to about 1.5 orbital periods of the binary. The observing run was short, lasting only three consecutive nights or five binary revolutions.

Figure 7 shows the ESP phase locations and phase evolution in AW UMa. The apparent equivalent of the single, well-defined feature in $\epsilon \text{ CrA}$, ESP#1, could be observed only on the first night at a similar sub-observer phase $\simeq 0.6 - 0.65$, as for $\epsilon \text{ CrA}$. It is possible that ESP#2 was a continuation of #1 on the two following nights; its velocities corresponded to the rotationally receding side of the secondary component. The features #3, #4 and #5 appeared at velocities similar to the presumed velocity of the secondary mass center. They tended to drift slightly on all three nights, with the region #5 being most stable at the mean velocity of the secondary. Finally, the repeatable and well-defined ESP#6 was observed at negative velocities; it was most probably produced by the matter moving along the surface of the secondary on its side approaching the observer.

While none of the ESPs can be explained within the Lucy model, the Stepień model actually *predicts* the existence of features such as those given numbers #1 and #6. The ESPs would be manifestations of the stream encompassing the binary system; the sufficiently spectral-line optically thick layers of the stream are visible emerging from behind the secondary component during the transit phases when they point at the observer and are visible as ESP#6. The stream continues around the secondary component and eventually strikes the outer layers of the primary, sending the hot gas into the overlying space; this region is visible as ESP#1 in AW UMa and as the corresponding single ESP in $\epsilon \text{ CrA}$. However, the ESP features close to the center of the AW UMa secondary profile do not have an explanation.

5. THE MASS-RATIO DISCREPANCY

There is a discrepancy in the mass-ratio determinations for AW UMa, with spectroscopic results (q_{sp}) consistently being larger than photometric results (q_{ph}). The new spectroscopic determination, as listed in Table 3, $q_{\text{sp}} = K_1/K_2 = 0.092 \pm 0.007$, is close to the previous David Dunlap Observatory medium-resolution determination by Pribulla & Rucinski (2008), $q_{\text{sp}} = 0.101 \pm 0.006$. The difference between the two determinations most likely reflects not only the use of different spectral resolutions

but also the very different temporal coverage during the two observing programs; the DDO result utilized 10 partial nights distributed over a longer interval in contrast to the short, intense, high-resolution run. Both spectral determinations are larger than several photometric determinations by different authors (see references in P1, particularly [Wilson \(2008\)](#)), some claiming errors as small as 0.0005 tending to concentrate around $q_{\text{ph}} = 0.080 \pm 0.005$.

The existence of a possible q_{ph} vs. q_{sp} discrepancy in AW UMa is important because the mass ratio is a fundamental parameter of a close binary system and plays a special role in the Lucy model in setting the value of the common equipotential. Indications of a possible discrepancy were signalled as early as [Niarchos & Duerbeck \(1991\)](#). At that time, spectroscopic determinations for W UMa binaries were lagging in both quantity and quality behind photometric Lucy-model determinations, as many spectral efforts were reduced to *spectroscopic detection* of faint secondary-component signatures. Some results appearing in the literature still used the inappropriate – for W UMa binaries – spectral “line-by-line” radial-velocity measurements. [Niarchos & Duerbeck \(1991\)](#) correctly explained the mass-ratio discrepancies as mainly due to poor accuracies of q_{sp} determinations of that time.

AW UMa was one of the first objects used to test modern spectroscopic techniques that utilized combined RV information from many spectral lines. This was mainly due to its brightness but also because of its unexpectedly small mass ratio indicated by the light-curve photometric solutions, $q_{\text{ph}} \simeq 0.08$. First attempts utilized the inherently non-linear Cross-Correlation Function (CCF) technique applied to also non-linear photographic data ([McLean 1981](#); [Anderson et al. 1983](#); [Rensing et al. 1985](#)). These were later replaced by a linear deconvolution (Broadening Function) technique applied to digital results ([Rucinski 1992](#)). Because of low detector sensitivity, limited large telescopes time, and the unexpectedly weak signature of the secondary component in AW UMa, early analyses were limited to confirming the photometric mass ratio. The first spectroscopic determination based on more extensive material by [Pribulla & Rucinski \(2008\)](#), $q_{\text{sp}} = 0.101 \pm 0.006$, clearly demonstrated that the mass ratio must be larger than previously thought. This result coincided with a theoretical analysis of [Paczynski et al. \(2007\)](#), which pointed out difficulties in explaining AW UMa as the result of the close binary-star evolution for $q < 0.10$.

A similar discrepancy as in AW UMa is very weakly evident for ϵ CrA, though still in the same sense, with $q_{\text{sp}} = 0.1300 \pm 0.0010$ (P2) compared with $q_{\text{ph}} = 0.114 \pm 0.003$ ([Twigg 1979](#)) and $q_{\text{ph}} = 0.1244 \pm 0.0014$ ([Wilson & Raichur 2011](#)). ϵ CrA may show partial eclipses so that its photometric determination of q_{ph} may be less reliable than for a totally eclipsing binary such as AW UMa.

A comparison of q_{ph} with q_{sp} utilizing much better data than those available to [Niarchos & Duerbeck \(1991\)](#) is now possible. A large body of spectroscopic determinations resulted from a program of RV observations of short-period ($P < 1$ day), bright binaries conducted in years 1993 – 2010 at the DDO and published in 23 papers in years 1993 – 2010. The program included 124 W UMa-type binaries. The spectroscopic determinations during the DDO program did not use any previous, literature data by design, ensuring no bias from published q_{ph} . The binaries were selected for observations based on the sky accessibility, star brightness, and the somewhat erratic weather conditions at the DDO. A list of the observed binaries is provided in [Rucinski et al. \(2013a, Table 1\)](#).

The size of the DDO spectroscopic program and the consistency of the methods used ensure uniformity of the q_{sp} determinations. In contrast, the photometric determinations come from various sources in the literature. All researchers utilized the light-curve synthesis model developed following the [Lucy \(1968b\)](#) description, which was first extensively used by [Mochnicki & Doughty](#)

Table 4. The q_{ph} and q_{sp} determinations of totally eclipsing systems

Name	$P(d)$	$B - V$	q_{ph}	σq_{ph}	q_{sp}	σq_{sp}	Refs.
<i>q_{sp} from the DDO survey</i>							
CC Com	0.2207	1.240	0.521	0.004	0.527	0.006	(1, 2)
V1191 Cyg	0.3134	0.390	0.094	0.005	0.107	0.005	(3, 4)
FG Hya	0.3278	0.540	0.138	0.009	0.112	0.004	(5,6,7, 8)
BB Peg	0.3615	0.480	0.356	0.003	0.360	0.009	(9, 8)
AM Leo	0.3658	0.490	0.398	0.003	0.459	0.004	(10, 2)
V417 Aql	0.3703	0.570	0.368	0.001	0.362	0.007	(11, 8)
HV Aqr	0.3745	0.470	0.146	0.020	0.145	0.050	(12, 13)
V566 Oph	0.4096	0.410	0.238	0.005	0.263	0.012	(5, 14)
Y Sex	0.4198	0.390	0.175	0.002	0.195	0.010	(15, 16)
EF Dra	0.4240	0.460	0.125	0.025	0.160	0.014	(17, 8)
AP Leo	0.4304	0.470	0.301	0.005	0.297	0.012	(18, 8)
AW UMa	0.4387	0.360	0.080	0.005	0.092	0.007	(19,20, 21,22)
DK Cyg	0.4707	0.380	0.330	0.020	0.325	0.040	(5, 23)
UZ Leo	0.6180	0.350	0.230	0.003	0.303	0.024	(24, 23)
<i>q_{sp} from other sources</i>							
RZ Com	0.3385	0.700	0.420	0.010	0.430	0.030	(25, 26)
AE Phe	0.3624	0.640	0.391	0.005	0.450	0.010	(27, 28)
AQ Tuc	0.5948	0.400	0.265	0.010	0.350	0.010	(29, 29)
RR Cen	0.6057	0.360	0.180	0.010	0.210	0.010	(5, 30)
MW Pav	0.7950	0.33	0.182	0.003	0.228	0.006	(31, 32)

NOTE— References to individual mass-ratio determinations (q_{ph} , q_{sp}):

1. Rucinski (1976), 2. Pribulla et al. (2007), 3. Pribulla et al. (2005), 4. Rucinski et al. (2008), 5. Mochnacki & Doughty (1972b), 6. Twigg (1979), 7. Yang et al. (1991), 8. Lu & Rucinski (1999), 9. Leung et al. (1985), 10. Hiller et al. (2004), 11. Samec et al. (1997), 12. Robb (1992), 13. Rucinski et al. (2000), 14. Pribulla et al. (2006), 15. Hill (1979), 16. Pribulla et al. (2007), 17. Plewa et al. (1991), 18. Zhang et al. (1992), 19. Mochnacki & Doughty (1972a), 20. Wilson & Van Hamme (2009), 21. Pribulla & Rucinski (2008), 22. Rucinski (2015)[P1], 23. Rucinski & Lu (1999), 24. Vinkó et al. (1996), 25. Wilson & Devinney (1973), 26. McLean & Hilditch (1983), 27. Niarchos & Duerbeck (1991), 28. Duerbeck (1978), 29. Hilditch & King (1986), 30. King & Hilditch (1984), 31. Lapasset (1980), 32. Rucinski (& Duerbeck(2006)

(1972a,b). The light-curve synthesis approach gained widespread utilization after its implementation by Wilson & Devinney (1973), followed by several widely accessible computer codes such as Wilson & Van Hamme (2009); Prša et al. (2016); Conroy et al. (2020); Wilson et al. (2020).

Certain precautions were applied to ensure the mutual independence of the q_{sp} and q_{ph} determinations. The selection included only: (1) W UMa-type binaries with q_{ph} Lucy-model determinations published *before* the spectroscopic determinations, and (2) binaries showing total eclipses to ensure the highest photometric solution stability irrespectively of the specific implementation of the Lucy model. The first condition aimed to prevent a “leak” and stabilization of the photometric, iterative,

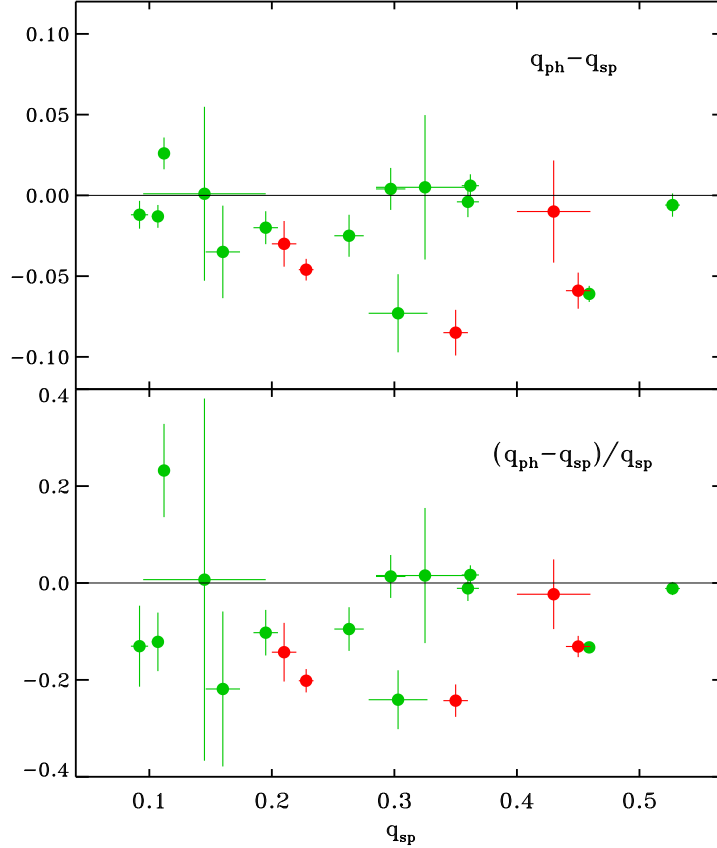


Figure 8. The mass-ratio discrepancy between the photometric, q_{ph} , and spectroscopic, q_{sp} , determinations is shown directly versus the spectroscopic value (the upper panel) and normalized by q_{sp} (the lower panel). The data shown in green correspond to q_{sp} determinations from the DDO survey while those in red are critically updated spectroscopic results listed by Niarchos & Duerbeck (1991). See the text for details.

multi-parameter solution on the already available spectroscopic value, while the second condition excluded poorly-conditioned light curve solutions based only on distortion effects. The selected binaries are listed in Table 4 which is similar to Table 2 in Niarchos & Duerbeck (1991).

The binaries with q_{sp} from the DDO program are marked in green in Figure 8 and listed in the first half of the table. We added binaries fulfilling the above restrictions from other sources, including the Niarchos & Duerbeck (1991) list, but only those with q_{sp} values determined using the CCF or BF deconvolution methods by other researchers. These results are listed in the second half of Table 4 and are marked by red symbols in the figure. Note that ϵ CrA is not included in the table since its primary eclipse may be partial or close to partial.

The difference $(q_{ph} - q_{sp})$ is shown in Figure 8 directly and, similarly as in Niarchos & Duerbeck (1991), in the relative sense, divided by the value of q_{sp} . The normalization is kept here to reflect our lack of knowledge on the source of the discrepancy. Regardless of the presentation, we observe a widespread occurrence of $q_{ph} < q_{sp}$, exactly as for AW UMa, which is the binary with the smallest q_{sp} in the figure. The size of the discrepancy is moderate, so either q_{sp} or q_{ph} could serve as an argument in the figure. The author believes that the spectroscopic q_{sp} results are currently better-defined because of their more straightforward derivation. We return to this subject in Section 7.

The only binary in Figure 8 showing the photometric value of q_{ph} larger than the spectroscopic q_{sp} is FG Hya. This binary has an extensive and consistent record of several photometric determinations, so it urgently requires a confirmation of the spectroscopic result. We note the spectroscopic result was obtained at the very beginning of the DDO program (Lu & Rucinski 1999).

The study of Niarchos & Duerbeck (1991) provided another strong indication that q_{ph} may be affected by phenomena not accounted in the photometric model. The light curve of AE Phe showed significant season-to-season changes, with one light curve showing a well-defined *total* occultation eclipse. The authors modeled the four seasonal curves using the Lucy model and found a range of q_{ph} results, from 0.3836 ± 0.0014 to 0.3964 ± 0.0010 . While the formal uncertainties are undoubtedly under-estimated, a difference of more than 0.01 between individual determinations of q_{ph} seems to be real and is highly concerning. Such a discrepancy would suggest a large and rapid mass exchange between the components, amounting to $0.01 M_{\odot}$, yet without an accompanying significant orbital-period variation.

The Stępień model (Section 7.2) offers a possible explanation for the transitions between rounded and flat-bottomed occultation eclipses in AE Phe. These variations could result from changes in the overall loading of the flow (also referred to as the “equatorial bulge”) around the secondary component. Unfortunately, no reliable q_{sp} determination is available for this star at present.

6. THE PHOTOMETRIC AND SPECTROSCOPIC MASS-RATIO DETERMINATIONS

The tendency for $q_{\text{ph}} < q_{\text{sp}}$ is an important indication that one of the methods used for mass-ratio determinations – either the photometric Lucy model or the spectroscopic direct approach – may produce systematically incorrect results. We note that the results of this study, along with those from our two previous papers, definitely confirm the existence of a velocity field in the rotating system of coordinates. Thus, strictly speaking, equipotentials cannot be defined. However, for low velocities, stellar shapes may still be close to predicted to the equipotential geometry. We return to this subject in Section 7.

The determination of photometric parameters for a W UMA-type binary is a complex process. Initially, a $3D \rightarrow 1D$ mapping of the stellar *brightness* (but not velocities) is performed by the revolving binary itself, which is registered as a light curve. This light curve is then subject to a multi-parameter solution utilizing the Roche-model geometry, with additional Lucy-model prescriptions for handling stellar-atmosphere properties. The solution is a highly non-linear, iterative process that includes unknowns such as the degree of contact (or the actual value of the common equipotential), and the orbital inclination, which are intermixed with assumed atmospheric properties, such as the local flux level estimated by surface brightness (effective temperature) and the limb and gravity darkening laws, typically derived from spherical stars. Due to inherent nonlinearities, this parameter determination process is highly susceptible to biased estimates and may result in deceptively small uncertainties when estimated as if for a linear, correlation-free problem based on the shape of the adopted deviations minimum. Unfortunately, this can lead to popularly quoted but suspiciously small formal uncertainties.

The complexity of photometric determination of q_{ph} can contribute to the observed q_{ph} vs. q_{sp} discrepancy. Eclipse effects carry relatively more information than the strongly model-dependent stellar-distortion effects. For spherical stars, it is known that the radius ratio, $k = r_2/r_1$ (Russell 1912), is the key parameter controlling the depth and shape of eclipses. Although the binary compo-

nents in our case are not spherical stars, an equivalent of k exists, albeit hidden within complexities of light-curve-synthesis codes. The individual dimensions of Roche common equipotential surfaces, expressed, for example, as side equatorial radii r_1 and r_2 , depend solely on the mass ratio, $r = r(q)$. This relation is known to be non-linear. A simplified version of it has been extensively used by practitioners of close-binary evolutionary calculations to estimate the size of the Roche-lobe (inner critical equipotential) filling component. In the orbital separation units, $r = 0.38 + 0.2 \log(q)$; this equation works for both components (with inverted q) and has an asymptotic low mass-ratio extension (Paczyński 1971, Eq.4). By being approximately logarithmic, the dependence $r = r(q)$ is a slowly-varying function. The weak dependence of the Roche-lobe radii on q is convenient for stellar binary models. However, q_{ph} determination utilizes an inverse relation, which – consequently – is a rapidly varying function. For the approximation as above, it is an *exponential* function, $q = 10^{5r-1.9}$. Therefore, small errors in the relative radius determination produce large deviations in the estimated mass ratio. An error of 1% in r produces a 4% error in an q_{ph} estimate.

The mass ratio is not determined from the sizes of the individual Roche equipotentials, but from the ratio of their radii, $k = r_2/r_1$. This reduces the exponential nature of the relationship, making the non-linearity milder. Using the same approximation for the inner critical Roche lobe as mentioned earlier, an approximate relation for the whole range $0 < k < 1$ remains nonlinear, $q \simeq k^{+2.23 \pm 0.03}$. Therefore, a 1% error in k is expected to produce a 2.2% error in q_{ph} .

The non-linearity in the q_{ph} determination, as described above, has not yet been recognized. A more concerning issue is the *tendency* for $q_{\text{ph}} < q_{\text{sp}}$ among individual binaries (Section 5), with some binaries exhibiting this behavior while others do not. While we believe that an incorrect photometric model is the reason, some photometric solutions may provide systematically smaller values of q_{ph} due to the presence of an unrecognized “third light” in the light curve. Companions to W UMa binaries are very common, as demonstrated by Tokovinin et al. (2006) and Rucinski et al. (2007). A light curve containing unrecognized additional light has a reduced amplitude and may result in a q_{ph} value that is too small. That was the case for the photometric solution of one of our two targets, ϵ CrA, analyzed by Shobbrook & Zola (2006); they commented on difficulties in obtaining the best fit starting from the assumed (and correct) spectroscopic value of $q_{\text{sp}} = 0.129$ (Goeking & Duerbeck 1993), being forced to reduce q_{ph} by 0.02. ϵ CrA is not listed in Table 4 precisely because it does not show total eclipses and therefore cannot provide a secure radius-ratio determination.

The spectroscopic approach offers an entirely different and independent route of the mass ratio determination involving a $3D \rightarrow 2D$ mapping, from the spatial velocities into a series of RV profiles arranged in time. This approach utilizes more accessible information in two dimensions of the time and radial velocity; the RV data provide the orbital semi-amplitudes K_1 and K_2 leading to $q_{\text{sp}} = K_1/K_2$. For very tight orbits, as observed for the W UMa-type binaries, with strongly dissipative, gaseous bodies involved, the only permitted orbits are circular, so that the derivation of the semi-amplitudes is particularly simple.

Although the direct approach using velocities suggests a lesser risk of biased results for the spectroscopic q_{sp} , the values of the amplitudes K_i may still be biased for other reasons. Paradoxically, the K_2 amplitude, which was very hard to determine in our binaries, seems to be more reliable, but only under strict conditions on the spectral feature used for the K_2 estimate. The feature: (1) must be free of any component profile overlap, (2) must move with the orbital phase in a sinusoidal manner,

(3) and strictly in anti-phase to the motion of the primary component. Obviously, any inter-binary velocity features must be entirely avoided.

In contrast to K_2 , the primary component velocity amplitude K_1 appeared deceptively easy to determine in both binaries analyzed here. The primary profiles seemed symmetric and straightforward to approximate using the classical rotational profile. However, it is unclear whether the profile center accurately traces the motion of the mass center, due to the distortion of the primary component. In both binaries, the small $v \sin i$ width variation due to the symmetric term of the simplified Roche potential expansion, $J = 2$ (e.g. Eq.(2) in Rucinski (1969)) was estimated at $\leq 5 \text{ km s}^{-1}$ (item #2 in the list in Section 2). The first asymmetric term ($J = 3$) is expected to be smaller by a factor of roughly r/a compared to the dominant tidal elongation term, where r is the primary mean radius and a is the mass center separation. The expected shift, $< 1.5 - 2.0 \text{ km s}^{-1}$, would lead to a systematic error $\delta(q_{\text{sp}}) \simeq 0.007$. Notably, due to the sense of the Roche-lobe asymmetry, this error would be opposite to that suggested by small value of q_{ph} , i.e. the actual K_1 of the mass centre (and thus q_{sp}) would be *larger* than estimated for the symmetric profile.

7. THE W UMA-TYPE BINARY MODEL

7.1. *The Lucy model*

When it appeared more than half a century ago, the Lucy (1968a,b) model was the first consistent description of W UMa binaries as dynamically stable configurations of solar-type stars in strong physical contact. The Lucy publication left important structural and energy-related issues open, but the light-curve calculation prescription was very convincing and simple: it suggested that common equipotentials of the Roche binary model as better describing components of W UMa binaries than – then used – complex descriptions of large tidal distortions imposed on spherical stars. While the unprecedented idea of two different-mass stars touching each other – and still in equilibrium – was not accepted immediately, the model found enthusiastic approval among binary-star observers interpreting light curves. The model perfectly reproduced the observed light curves, assuming that both stars had identical surface brightnesses. The particularly successful work on totally eclipsing W UMa-type binaries by Mochnacki & Doughty (1972a,b) followed by similar investigations by Lucy (1973) and Wilson & Devinney (1973) showed the great potential in that domain. The Lucy prescription found widespread use when ready-made, easy-to-install codes became widely available thanks to the generosity of several investigators (Wilson & Van Hamme 2009; Prša et al. 2016; Wilson et al. 2020; Conroy et al. 2020). There were voices of a rather low information content of the light curves (Rucinski 1993, 2001) and of a sensitivity to the ubiquitous presence of third stars (Rucinski et al. 2007), but they were ignored.

Interpretation of the W UMa-type binary light curves unambiguously shows that the surface brightnesses of both components are almost perfectly the same, despite commonly observed mass ratios different from unity, sometimes as small as $q \simeq 0.1$, as for our stars or smaller (Wadhwa et al. 2021; Li et al. 2022; Guo et al. 2023). For Main Sequence stars, the ratio of nuclear luminosities scales as $L_2/L_1 \propto q^\alpha$ with $\alpha \simeq 4 - 5$ so that the secondary components in most cases would be expected to be energetically inert stars. To explain the observed equal-temperature property, Lucy (1968a) proposed the turbulent, gravity-driven convection – known for its high efficiency in solar-type stars – as a process carrying colossal amounts of energy from the primary to the secondary component. This assumption was entirely *ad hoc* and most likely incorrect: the force driving convection is directed

perpendicularly to the direction of energy transport in the volume between the two stars; therefore, turbulent convection is expected to be entirely extinguished there or to carry insignificant amounts of energy. A more likely seemed to be an organized flow deep in the stellar interior as suggested by [Webbink \(1976, 1977\)](#); however, existing descriptions still did not include the weak, but ever-present Coriolis force. In both mechanisms, by Lucy and by Webbink, an assumption was made of energy transport originating in the primary component core and depositing the energy deep inside the secondary. Thus, both can be called the “internal” energy-transport solutions.

An “external” process was proposed by [Shu et al. \(1976\)](#). The authors pointed out that the faster evolutionary expansion of the more massive component may lead to a “boiling over” of the primary-component matter onto the secondary, resulting in a complete enshrouding of the secondary component by the hotter gas. The same matter would then be visible over the whole binary surface. This would perfectly explain the observed temperature equality, but – contrary to normal conditions in external layers of stars – the hot material would have to stably stay on the cooler gas of the secondary. The inverted-temperature solution was strongly criticized as containing deep physical problems and has been abandoned ([Papaloizou & Pringle 1979](#); [Shu et al. 1979](#)).

The review by [Smith \(1984\)](#) summarized the theoretical difficulties of the Lucy model, particularly the over-constrained nature of its structural assumptions and the lack of a credible energy-transfer mechanism. Following remarks by [Webbink \(2003\)](#) on the lack of new theoretical research, subsequent investigations primarily focussed on binary evolution issues. [Yakut & Eggleton \(2005\)](#) presented a comprehensive discussion of differential evolution as a factor providing stability for W UMa-type systems consisting of stars of different masses. However, research on energy transport between the components has stagnated, even as the Lucy photometric model has continued to successfully reproduce large numbers of observed light curves. Through its frequent and extensive use, all aspects of the Lucy model gradually gained general acceptance, and the unresolved issue of energy transfer ceased to be discussed.

7.2. *The Stępień model*

The [Stępień \(2009\)](#) model of W UMa-type binaries focuses on an aspect largely ignored in the Lucy model: the solution for the energy flow between the components with a particular attention to the Coriolis force, which organizes the flow and makes it concentrated to the equatorial regions. The model predicts inter-binary velocities so that the Roche equipotentials cannot be defined. However, for sufficiently small velocities, gravity and centrifugal forces dominate, restoring the geometrical properties often described by the term of the “Roche lobes”. The Stępień model offers a wide range of solutions for W UMa-type binaries formed from differentially evolved components and observed as various subclasses of such systems ([Stępień & Kiraga 2013](#)).

As a starting point, the [Stępień \(2009\)](#) model utilizes results from detailed hydrodynamical calculations by [Oka et al. \(2002\)](#), who analyzed the velocity field on a Roche-lobe-overflowing component in a close binary system. The original calculations involved a different scenario than a W UMa binary: a mass-losing component in a cataclysmic binary transferring matter into the deep potential well of a massive, very small (collapsed) star. The important hydrodynamical details of the initial stages of the outflow are expected to be very similar, irrespective of the nature of the mass gainer. In the case of the Stępień model, the binary components have been brought into contact by magnetic wind and tidal dissipation processes. The mass-losing primary is assumed to be a Main Sequence star, possibly showing some evolution. In fact, the primaries of the AW UMa and ϵ CrA systems clearly show a

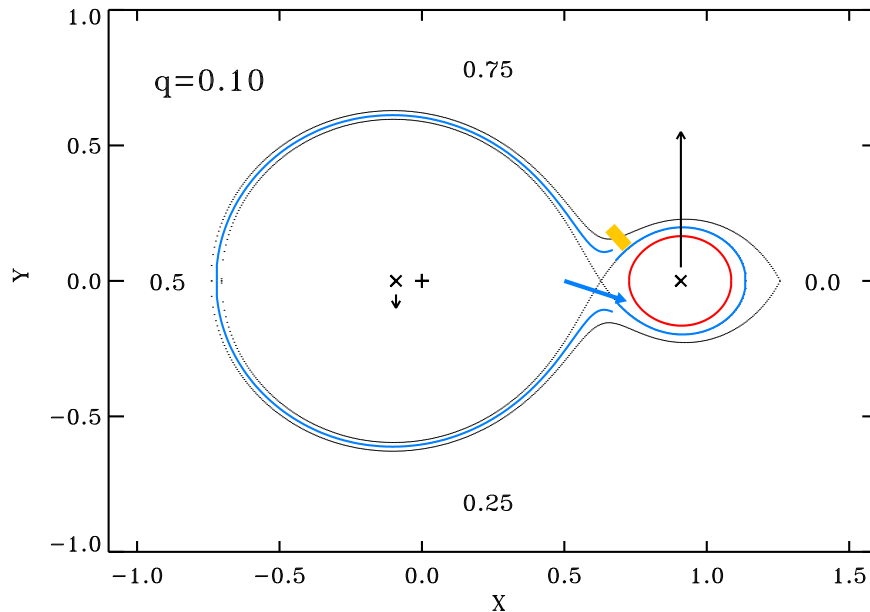


Figure 9. Properties of the Stępień (2009) model follow consideration of the initial stages of the Roche-lobe overflow by the primary. The flow is deflected by the Coriolis force to the side of the secondary, building up a thick belt. The shape of the belt in the orbital plane may be close to an equipotential but different from that describing the primary component and very likely tighter. As a result, one component slightly overfills and the other slightly underfills the Roche model common equipotential. The figure is for $q = 0.10$, similar to that of AW UMa and ϵ CrA. The blue line shows the hot gas of the expanding primary, while the secondary component is shown in red. The approximate location of the prominent Enhanced Spectral-line Perturbation (ESP) observed in both binaries is marked in orange. The numbers at the perimeter give the orbital phase positions of an external observer. The arrows at the mass centers represent (in scale) the orbital velocities of the component stars.

different advancement in the evolution. The binary is, therefore, of the SD1 type in the classification of Yakut & Eggleton (2005).

The primary transfers its matter to the less-massive secondary, which is expected not to expand excessively during the process. This suggests that the secondary is a low-mass star or the core of a mildly evolved MS star, possibly resulting from a previous binary mass exchange or a component exchange in a triple system. The stream from the primary is massive and forms an equatorial “bulge” on the secondary. Its equatorial extension is subject to the binary gravitational forces, allowing it to fill the entire critical lobe of the star. As observed more clearly in the case of ϵ CrA (Figure 2), the flow appears to exhibit a range of rotational velocities similar to that of a Roche-model-filling secondary at phases around $\phi \simeq 0.25$, but it settles to a smaller velocity range at the $\phi \simeq 0.75$ half of the orbit. We note that the secondary component’s signature is very difficult to observe leading to a particularly large measurement scatter in Figures 2 and 7.

While the photospheric sound velocity for F-type stars, such as the AW UMa and ϵ CrA primaries, is of the order 7 km s^{-1} , the energy-carrying flow originates in sub-photospheric layers, where velocities may reach $30 - 50 \text{ km s}^{-1}$. These velocities remain small relative to free-fall or orbital velocities, so gravitational forces still dominate in controlling the geometric properties of the flow and the overall geometry does not deviate appreciably from the Roche model. The flow is confined to the equatorial regions. It continues around the secondary and returns to the primary. At all phases, the matter

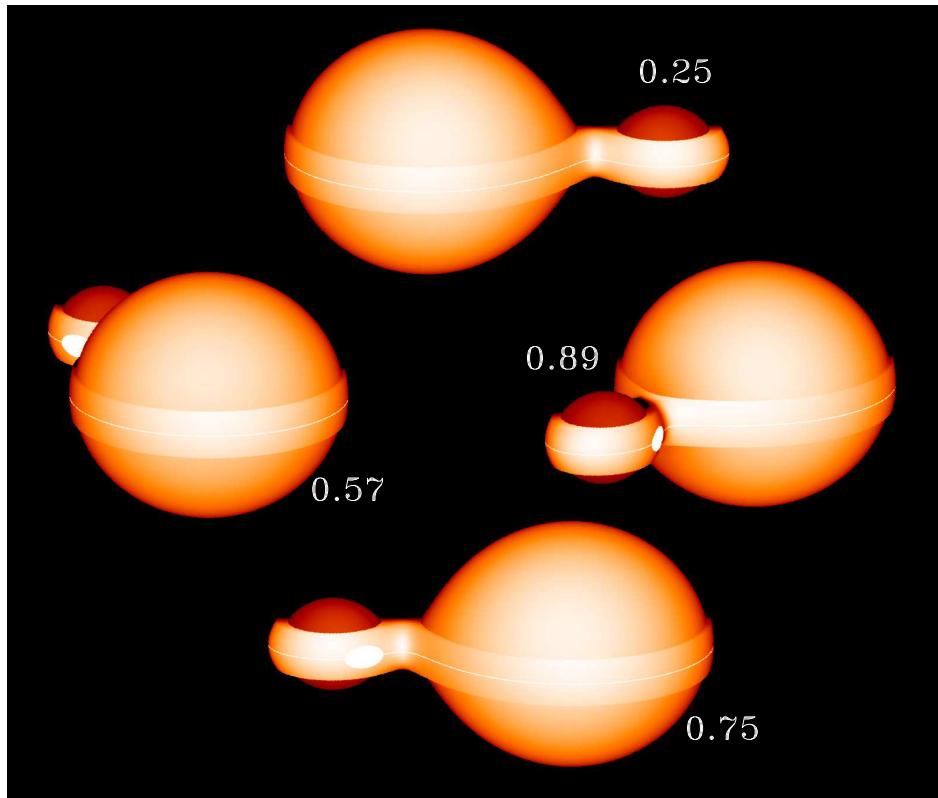


Figure 10. A schematic view of ϵ CrA at four orbital phases envisaged for the Stępień model; compare it with Figure 3 for the Lucy model. The belt surrounding both stars is pictured here with an arbitrary height of ± 0.1 orbital separation units; its temperature is set slightly higher than at the side of the primary for better visibility while the secondary is cooler. For a simpler visual representation, all shown surfaces follow the equipotentials: the primary is at the inner critical one, the secondary at the one with the side radius 0.95 of its inner critical, while the belt is positioned at a half-way between the inner and outer critical equipotentials.

from primary component dominates the external view of the binary. The actual secondary star may be almost entirely hidden within the flow. The changing orbital aspect and eclipses of the flow are observed as the W UMa-type variability. The binary would be expected to look very differently at large inclinations, but in such cases, it would not be detected as a variable star.

Upon leaving the primary, the gas flow – starting with moderately supersonic velocities – is deflected by the Coriolis force to the side of the secondary. This area may be visible as a hot spot and manifest itself as the O’Connell effect in the light curve. The binary V361 Lyr (Hilditch et al. 1979) is currently the best-known example where the deflection of the stream and interaction with the local matter is strongly manifested. This side of the binary corresponds to that visible at $\phi = 0.25$ in AW UMa and ϵ CrA (Figure 9). The flow and its impact appear to have been also observed at a moderate spectral resolution in the massive W UMa binaries strongly showing the O’Connell effect, such as DU Boo and AG Vir, as noted by Pribulla et al. (2011).

Most of the transferred matter completes only a single revolution around the secondary before striking the primary’s atmosphere on the side visible in the $\phi = 0.75$ hemisphere. This is where we observe the prominent Enhanced Spectral-line Perturbation (ESP), which is visible in both binaries discussed in this paper, projecting against the secondary profile at the sub-observer at the same

phase, $\phi \simeq 0.65$ (marked in orange in Figure 9). It is important to stress that we see the ESPs as regions of an increased line-of-sight atom density, rather than as hot or cool spots.

While part of the flow may end up on the primary component at that point, the flow may continue around both components and may be visible as the “pedestal” of the primary-component profile (item 1. in the list in Section 2). Thus, at all phases, the light curve of a binary is dominated by two sources: the primary itself and the flow of matter encompassing the whole binary, originating from the primary. The secondary may be entirely invisible, or it may heat up to an equilibrium with the overlying equatorial belt due to a “bottling-up” effect of its own energy, constrained by a narrow polar opening, as described by [Stepień \(2009\)](#).

As described above, the flow retains relatively low velocities compared to those needed to restore the dynamical equilibrium in the binary. Its motion around the secondary continues to be subject of energy and angular-momentum losses due to very strong tides within the secondary component’s lobe. These forces should extract the kinetic energy of the flow and send the material “down”, closer to the surface of the secondary component. Thus, the model offers a prediction which may be observed as the q_{ph} vs. q_{sp} discrepancy (Section 5): While typically, we expect that the primary component *to exceed* the critical-lobe dimensions for the given mass ratio, the transferred matter may end on an orbit around the secondary of *smaller dimensions* than the critical lobe (Figure 9). This would be only a *tendency*, depending on the stage of binary evolution for a particular case and the intensity of the mass flow. It is important to stress that, in the case of the new model, the photometric mass ratio are determined from the shape of the flow, not from dimensions of the underlying stars. Thus, any variations of q_{ph} , as described by [Niarchos & Duerbeck \(1991\)](#) for AE Phe, would probably indicate variations in the shape or mass-loading of the flow.

The [Stepień \(2009\)](#) model may find particularly fertile ground for spectroscopic high-resolution investigations among the “poor thermal contact binaries”, i.e. , binaries as close as those of the W UMa-type but with components of unequal temperatures. In such binaries, the flow is clearly unable to transfer the energy between the components. These binaries are usually the most unstable, as if seeking a new equilibrium state. [Siwak et al. \(2010\)](#) conducted a combined photometric/spectroscopic investigation of several of such binaries using the best currently available techniques. The spectroscopic data show well-defined profiles of cool and faint secondary components and the presence of strong ESP features visible on the $\phi = 0.75$ hemisphere. CX Vir was most extensively observed: The “phase 0.65” ESP feature in that binary does not seem to look the same as in AW UMa and ϵ CrA; it is much stronger and seems to show a different phase-drift dependence. Firm conclusions from the excellent CX Vir data are hard to derive because the sparse phase coverage in the [Siwak et al. \(2010\)](#) paper is limited to narrow intervals around the orbital quadratures. We can recognize the features interpretable by the Stepień model, but the details seem to be different.

8. CONCLUSIONS

The paper contains a combined discussion of the previously obtained results for the two W UMa-type binaries, AW UMa (P1) and ϵ CrA (P2). Both binaries were monitored over time at high spectral resolution, and they share many physical properties, notably the very small mass ratio and early-F spectral type. Their similarity largely stems from the availability of instrumentation but has revealed interesting and unexpected details discussed in this paper. Additionally, the later analysis of ϵ CrA, which is a simpler binary, helped to interpret unexplained features observed in AW UMa in P1.

Both binaries – particularly AW UMa – have been repeatedly observed photometrically, and their light curves perfectly agree with the common-equipotential light-curve-synthesis model of Lucy (1968a,b). However, the spectroscopic perspective presents a more complex picture of a circumbinary flow with velocities not exceeding $30 - 50 \text{ km s}^{-1}$. Such velocities, moderate compared to the free-fall or orbital velocities of about $300 - 350 \text{ km s}^{-1}$, are predicted in the Stępień (2009) energy transport model of W UMa binaries. This model envisages an optically thick stream or belt of matter originating from the Roche-lobe-overflowing primary component, which retains its heat during the transport (Section 7.2). The observed W UMa-type variations result from the changing visibility and eclipses of this energy-carrying belt, whose eclipse and visibility-aspect variations closely resemble those of the Roche model geometry.

We note (Figure 2) that the observed rotational velocities of the ϵ CrA secondary are very similar to those expected for a rigidly rotating Roche model in the first half of the orbit ($\phi = 0.25$). In contrast, the second half of the orbit ($\phi = 0.75$) shows possible settling of the velocities to lower rotational velocities. This behavior is exactly as predicted for a flow that initially fills the critical lobe and then loses its energy, drifting closer to the secondary’s otherwise invisible surface. The same effect is not as clearly visible in the much more complicated case of AW UMa (Figure 7), which was also a less-well observed binary.

The new results for AW UMa confirm the “large” value of the spectroscopically determined mass-ratio $q_{\text{sp}} = 0.092 \pm 0.007$ (Section 4), in contrast to the often quoted photometrically derived value, $q_{\text{ph}} = 0.080 \pm 0.005$ (this error comes from a scatter of several independent solutions). The new determination agrees with the previous spectroscopic result obtained at a medium spectral resolution, $q_{\text{sp}} = 0.101 \pm 0.006$ (Pribulla & Rucinski 2008). The difference in spectral resolutions is important, as it relates to the different ways of measuring the secondary component’s orbital semi-amplitude K_2 . The high spectral resolution result is based on the very weak, almost flat profiles of the AW UMa secondary, with an attempt not to include the Enhanced Spectral-line Perturbation (ESP) features. In contrast, the previous medium-resolution measurements included the then-unrecognized ESPs in the averaged secondary profiles. The ESPs are not hot or cool regions but rather volumes of increased line-of-sight densities of atoms, having excitation properties similar to those of the primary component’s outer regions. The AW UMa secondary typically shows two to four such localized ESPs, which are seen migrating as the binary rotates, projecting onto the secondary profile. In both binaries, one strong ESP was localized in the region between the stars, projecting on the secondary component profile at the sub-observer orbital phase $\phi = 0.65$. Such location is expected in the Stępień model as a place where the returning stream collides with the primary component after revolving around the secondary.

The difference between ϵ CrA and AW UMa in the number of ESPs currently lacks an explanation. While the ESPs are most likely driven by local thermodynamical instabilities and are chaotic in nature, it is possible that the two binaries differ in the type or extent of the flow. The stronger ESP variability in AW UMa may indicate that the flow around its secondary, as envisaged in the Stępień model, is more erratic than that in ϵ CrA or is subject to a localized pileup. We also note opposite tendencies in the systematic orbital-period changes of the two binaries (Section 2):

Based on the sign of the period changes, the *net mass exchange* between the components of AW UMa appears to be directed from the more massive primary to the less massive secondary, whereas in ϵ CrA, it flows in the opposite direction. One possible explanation is that the multitude of ESPs on the AW

UMa secondary signals an "overload" of the flow, caused by the abundance of incoming matter at this particular stage of binary evolution

The confirmation of the $q_{\text{ph}} < q_{\text{sp}}$ inequality in AW UMa, along with the absence (or small size) of a similar discrepancy in ϵ CrA, prompted an analysis of several binaries with the best-constrained photometric solutions in Section 5. A careful selection of W UMa binaries with spectroscopic q_{sp} determinations and the best (total eclipse) Lucy-model photometric solutions indicates that discrepant results are common and that smaller values of q_{ph} are a persistent tendency (Section 5, Figure 8). This could be explained within the [Stępień \(2009\)](#) model as due to the tight circulation of the energy-transporting belt around the secondary component, in contrast to the Roche-lobe overfilling primary. Thus, the two stars are expected to show opposite tendencies for deviations from the common equipotential of the Lucy model; this, in turn, could lead to a smaller value of q_{ph} than the real one.

While the [Stępień](#) model may suggest directions for exploring the $q_{\text{ph}} < q_{\text{sp}}$ tendency, it does not provide predictions regarding the magnitude of deviations from the Lucy model or suggest methods to reconcile q_{ph} or q_{sp} results. Currently, the photometric approach dominates, utilizing complex, state-of-the-art light-curve synthesis codes ([Prša et al. 2016](#); [Conroy et al. 2020](#); [Wilson et al. 2020](#)) which have largely superseded earlier explorations based on based on ASAS ([Pilecki 2009](#)), OGLE ([Soszyński et al. 2015](#)) surveys, and the extensive compilation of nearly 700 results by [Latković et al. \(2021\)](#). A convenient tool for a large-scale handling of statistical q_{ph} data – implicitly assuming a strict acceptance of the Roche model – has already been developed by [Pešta & Pejcha \(2023\)](#). But do summaries combining q_{ph} and q_{sp} data, such as those by [Gazeas & Stępień \(2008\)](#), [Latković et al. \(2021\)](#) or [Gazeas \(2024\)](#), provide an unbiased picture?

New spectroscopic investigations of W UMa-type binaries are urgently needed. Observations of AW UMa at two spectral resolutions suggests that medium-resolution ($R \simeq 15,000 - 20,000$) data may suffice for an acceptable determination of q_{sp} . However, detailed analysis of spectral profiles and detection of ESPs require a higher resolution ($R > 30,000$). The binary FG Hya ($V \simeq 10$, $q_{\text{sp}} = 0.14$) is the only case of the inverted mass-ratio discrepancy (Section 5, Figure 8), and it urgently requires a new spectroscopic determination. Binaries with less extreme mass ratios particularly need spectroscopic work: we already have tantalizing indications ([Pribulla et al. 2006](#); [Pribulla & Rucinski 2008](#)) that medium-resolution RV profiles for V566 Oph ($V \simeq 7.5$, $q_{\text{sp}} = 0.263 \pm 0.012$) look – unlike those of our two binaries – as predicted by the Lucy model. Interpreted within the [Stępień](#) model, this may indicate that the circumbinary flow fully dominates the spectroscopic profile shape for V566 Oph, in contrast to our two, very low mass-ratio systems where the primaries are dominant. It is possible that the flow dominance is a typical situation for W UMa binaries with mass ratios larger than some specific value. We note that the two binaries considered here are not cases of extremely small q_{ph} , as smaller values have already been reported in the literature ([Wadhwa et al. 2021](#); [Li et al. 2022](#); [Guo et al. 2023](#)).

At the other end of the mass ratio range, two moderately bright W UMa binaries would be particularly important for a broader spectroscopic picture: SW Lac ($V \simeq 8.7$) with $q_{\text{sp}} = 0.776 \pm 0.012$ ([Rucinski et al. 2005](#)) and OO Aql ($V \simeq 9.5$) with $q_{\text{sp}} = 0.846 \pm 0.007$ ([Pribulla et al. 2007](#)). We noticed during the DDO program that the RV profiles of SW Lac have shapes very much like those of a genuine semi-detached system (SD2), yet with components having identical atmospheric properties. Finally, the poor thermal contact binaries (Section 7.2), particularly the bright ones previously

analyzed by [Siwak et al. \(2010\)](#), may – when observed spectroscopically over all orbital phases – show more details of the flow. Possibly the flow is too weak to engulf the equatorial regions of the secondary yet strong enough to produce the already observed, prominent ESP features.

For a final summary: While spectroscopy is essential for our understanding of W UMa binaries, it remains difficult and costly. We have some insight into how these binaries form in small stellar groups and that they likely consist of differentially evolved components. However, we are still in the early stages of understanding the structure and surprising stability of these binaries. The roles of tidal energy and angular momentum dissipation remains to be studied and incorporated into models similar to those of [Oka et al. \(2002\)](#). Such models could help in interpreting spectroscopic results, partly regarding the complex velocity fields observed within these binaries.

ACKNOWLEDGMENTS

I would like to thank Dr. Andrej Prša who, acting as a reviewer of the paper, suggested important improvements and corrections to the text.

I would like to thank Staszek Zoła and Michał Siwak for useful suggestions and comments.

Special thanks go to Kazik Stępień, the originator of the new model for W UMa binaries for his insightful ideas, interesting discussions, and suggestions on the presentation of arguments.

REFERENCES

- Anderson, L., Stanford, D., & Leininger, D. 1983, *ApJ*, 270, 200
- Conroy, K. E., Kochoska, A., Hey, D., et al. 2020, *ApJS*, 250, 34
- Duerbeck, H. W. 1978, *AcA*, 28, 49
- Gaia Collaboration EDR3, 2020, *A&A*, 649A, 1
- Gazeas, K. 2024, *Contr. Astr. Obs. Skalnaté Pleaso*, 54, 58
- Gazeas, K. & Stępień, K. 2008, *MNRAS*, 390, 1577
- Gies, D. R., Bagnuolo, W. G., & Penny, L. R. 1997, *ApJ*, 479, 408
- Goecking, K.D., & Duerbeck, H.W. 1993, *A&A*, 278, 463
- Guo, D.-F., Li, K., Liu, F., et al. 2023, *MNRAS*, 521, 51
- Hilditch, R. W. & King, D. J. 1986, *MNRAS*, 223, 581
- Hilditch, R. W., Cameron, A. C., Hill, G., Bell, S. A. & Harries, T. J. 1997, *MNRAS*, 291, 749
- Hill, G. 1979, *Publ. DAO*, 15, 297
- Hiller, M. E., Osborn, W., & Terrell, D. 2004, *PASP*, 116, 337
- King, D. J. & Hilditch, R. W. 1984, *MNRAS*, 209, 645
- Lapasset, E. 1980, *AJ*, 85, 1098
- Latković, O., Čeki, A., & Lazarević, S. 2021, *ApJS*, 254, 10
- Leung, K.-C., Zhai, D., & Zhang, Y. 1985, *AJ*, 90, 515
- Li, K., Gao, X., Liu, X.-Y., et al. 2022, *AJ*, 164, 202
- Linder, N., Rauw, G., Sana, H., De Becker, M., and Gosset, E.. 2007, *A&A*, 474, 193
- Lu, W. & Rucinski, S. M. *AJ*, 118, 515
- Lucy, L. B. 1968a, *ApJ*, 151, 1123
- Lucy, L. B. 1968b, *ApJ*, 153, 877
- Lucy, L. B. 1973, *Ap&SS*, 22, 381
- McLean, B. J. 1981, *MNRAS*, 195, 931
- McLean, B. J. & Hilditch, R. W. 1983, *MNRAS*, 203, 1
- Mochmacki S.W., & Doughty N.A. 1972a, *MNRAS*, 156, 51
- Mochmacki S.W., & Doughty N.A. 1972b, *MNRAS*, 156, 243
- Niarchos, P. G. & Duerbeck, H. W. 1991, *A&A*, 247, 399
- Oka, K., Nagae, T., Matsuda, T., et al. 2002, *A&A*, 394, 115
- Paczyński B. 1964, *AJ*, 69, 124
- Paczyński B. 1964, *ARA&A*, 9, 183
- Paczyński B., Sienkiewicz, R., & Szczygieł, D. M. 2007, *MNRAS*, 378, 961
- Papaloizou, J. & Pringle, J. E. 1979, *MNRAS*, 189, 5P
- Pešta, M & Pejcha, O. 2023, *A&A*, 672, A176
- Pilecki, B. 2009, PhD Thesis, Warsaw University (unpublished)
- Plewa, T., Haber, G., Włodarczyk, K. J., & Krzesiński, J. 1991, *Acta Ast.*, 41, 291
- Pribulla, T., & Rucinski, S. M. 2008, *MNRAS*, 386, 377
- Pribulla, T., Vaňko, M., Chochol, D., et al. 2005, *Ap&SS*, 296, 281
- Pribulla, T., Rucinski S. M., Lu, W., et al. 2006, *AJ*, 132, 769
- Pribulla, T., Rucinski S. M., Conidis, G., et al. 2007, *AJ*, 133, 1977
- Pribulla, T., Rucinski S. M., Blake, R. M., et al. 2009, *AJ*, 137, 3655
- Pribulla, T., Vaňko, M., Chochol, D., et al. 2011, *Astronomische Nachrichten*, 332, 607
- Prša, A., Conroy, K. E., Horvat, M., et al. 2016, *ApJS*, 227, 29.
- Rensing, M. J., Mochmacki, S. W., & Bolton, C. T. 1985, *AJ*, 90, 767
- Rieutord, M., Petot, P., Reese, D., et al. 2023, *A&A*, 669, A99
- Rieutord, M., Reese, D. R., Mombarg, J. S. G., & Charpinet, S. 2024, *A&A*, 687, A259
- Robb, R. M. 1992, *Inf. Bull. Variable Stars*, No. 3798
- Rucinski S. M. 1969, *AcA*, 19, 125
- Rucinski S. M. 1976, *PASP*, 88, 777
- Rucinski S. M. 1992, *AJ*, 104, 1968
- Rucinski S. M. 1993, *PASP*, 105, 1433
- Rucinski S. M. 2001, *AJ*, 122, 1007
- Rucinski, S. M. 2002a, *PASP*, 114, 1124
- Rucinski, S. M. 2002b, *AJ*, 124, 1746
- Rucinski, S. M. 2010, in *Binaries – Key to Comprehension of the Universe*, eds. A. Prša, M. Zejda, *ASP Conf. Ser.* 435, 195
- Rucinski, S. M. 2012, in *From Interacting Binaries to Exoplanets: Essential Modeling Tools*, eds. M. Richards, & I. Hubeny *IAU Symp.*, 285, 365

- Rucinski S. M. 2015, *AJ*, 149, 49 (P1)
- Rucinski S. M. 2020, *AJ*, 160, 104 (P2)
- Rucinski, S. M. & Duerbeck, H. W. 2006, *AJ*, 132, 1539
- Rucinski, S. M., & Lu, W. 1999, *AJ*, 118, 2451
- Rucinski, S. M., Lu, W., & Mochnacki, S. W. 2000, *AJ*, 120, 1133
- Rucinski, S. M., Pych, W., Ogłóza, W., et al. 2005, *AJ*, 130, 767
- Rucinski S. M., Pribulla, T., van Kerkwijk, A. H. 2007, *AJ*, 134, 2353
- Rucinski S. M., Pribulla, T., Mochnacki, S. W., et al. 2008, *AJ*, 136, 586
- Rucinski, S. M., Pribulla, T., & Budaj, J. 2013a, *AJ*, 146, 70
- Rucinski S. M., Matthews, J. M., Cameron, C., et al. 2013b, *Inf. Bull. Var. Stars*, 6079
- Russell, H. N. 1912, *ApJ*, 36, 54
- Samec, R. G., Pauley, B. R., & Carrigan, B. J. 1997, *AJ*, 113, 401
- Shobbrook, R. R., & Zola, S. 2006, *Ap&SS*, 304, 43
- Shu, F. H., Lubow, S. H., & Anderson, L. 1976, *ApJ*, 209, 536
- Shu, F. H., Lubow, S. H., & Anderson, L. 1979, *ApJ*, 229, 223
- Siwak, M., Zola, S., & Koziel-Wierzbowska, D. 2010, *AcA*, 60, 305
- Smith, R. C. 1984, *QJRAS*, 25, 405
- Soszyński, I., Stępień, K., Pilecki, B., et al. 2015, *AcA*, 65, 39
- Stępień, K. 2009, *MNRAS*, 397, 857
- Stępień, K. & Kiraga, M. 2013, *AcA*, 63, 239
- Tapia, S. & Whelan, J., 1975, *ApJ*, 200, 98
- Tokovinin, A., Thomas, S., Sterzik, M., & Udry, S. 2006, *A&A*, 450, 681
- Twigg, L. W. 1979, *MNRAS*, 189, 907
- Vinkó, J., Hegedüs, T., & Hendry, P. D. 1996, *MNRAS*, 280, 489
- Wadhwa, S.S., De Horta, A., Filipović, M.D., 2021, *MNRAS*, 501, 229
- Webbink, R. F. 1976, *ApJS*, 32, 583
- Webbink, R. F. 1977, *ApJ*, 215, 851
- Webbink, R. F. 2003, in *3D Stellar Evolution*, eds. S. Turcotte, S. C. Keller, R. M. Cavallo, *ASP Conf. Series*, 293, 76
- Wilson, R. E. 2008, *ApJ*, 672, 575
- Wilson, R. E., & Raichur, H. 2011, *MNRAS*, 415, 596
- Wilson, R. E., & Devinney, E. J. 1973, *ApJ*, 182, 539
- Wilson, R. E., & Van Hamme, W. 2009, *ApJ*, 699, 118
- Wilson, R. E., Devinney, E. J., & Van Hamme, W. 2020, *Astrophysics Source Code Library*. ascl:2004.004
- Yakut, K. & Eggleton, O. P. 2005, *ApJ*, 629, 1055
- Yang, Y.-L., Liu, Q.-Y., Zhang, Y.-L., & et al. 1991, *Acta Astron. Sinica*, 32, 326
- Zhang, J. T., Zhang, R. X., & Zhai, D. S. 1992, *Acta Astron. Sinica*, 33, 131 (*Chinese Astron. Astrophys.*, 16, 407))